POLYTECHNIC OF TURIN

Master's Degree in Aerospace Engineering

Politecnico
di Torino

Master's Degree Thesis

Design and Development of a Test Bench for LiPo Batteries for Residual Charge Capacity Prediction

Supervisors

Prof Giorgio GUGLIERI

Francesco MARINO

Candidate

Maradon HASANAJ

December 2023

"True knowledge comes from deep understanding and our ability to comprehend and apply information in meaningful ways."
— [Stephen Hawking]

Abstract

As the use of Unmanned Aerial Vehicles (UAVs), especially quadcopters, continues to surge, the performance of lithium-ion batteries becomes increasingly significant. These batteries not only influence the operational autonomy of UAVs but also determine the overall success and longevity of aerial missions. Motivated by the pressing need to accurately evaluate and predict battery behavior over its lifecycle, this thesis starts on the development of a test bench. This bench is specifically designed to develop a predictive model for LiPo batteries, shining a light on their residual charge capacity.

The study methodically outlines each step, from the initial design of the test bench to the selection of the right components, and finally, the software implementation. The rigor applied in this phase was indispensable, establishing foundational benchmarks for the study and ensuring that every data collection step was attuned to precision and reliability.

Post data collection, the research focused on developing a model capable at estimating the future energy capacity of these batteries. Results from this endeavor were revealing curves derived from experimental tests signaled a decline in performance as C-rate increased. Furthermore, an observed performance gap of 5 to 10% in capacity between two tested batteries, with larger discrepancies linked to higher C-rates, underscored the behavior of these energy components. Through the developed predictive model, the research could pinpoint the battery's lifespan.

Acknowledgements

I would like to begin by expressing my gratitude to Professor Guglieri and my supervisor Francesco for their support during the development of this thesis. I am thankful for the opportunity to work on a topic that has allowed me to learn and conduct data collection.

In this regard, I also extend my thanks to the members of Team DRAFT. Your reviews, valuable feedback, expertise, and the diverse perspectives you each contributed have been instrumental in shaping this work and have played a pivotal role.

I am grateful to my family for their patience and trust in me. It brings me joy to know that I have brought some pride to your hearts.

I lovingly dedicate this thesis to my grandmother. Your kindness, care, and unwavering support have been my source of strength throughout the years of pursuing my master's degree.

Lastly, I would like to thank my mother. This journey, challenging and demanding, has now come to an end. You have been my inspiration and strength to carry on. We have achieved this milestone together, and I know you will always be by my side, guiding me towards future goals.

Table of Contents

List of Figures

Acronyms

EV
Electric Vehicles

Li-ion
Lithium-ion

SEI
Solid Electrolyte Interphase

SOH
State of Health

IR
internal resistance

UAV
Unmanned Aerial Vehicle

LiPo
Lithium-ion polymer

LIB
Lithium-ion battery

PE
Positive Electrode

NE
Negative Electrode

LAM

Loss of Active Material

LLI

Loss of Lithium Inventory

PCB

Printed Circuit Board

ESC

Electronic Speed Controller

DC

Direct Current

AC

Alternating Current

PWM

Pulse Width Modulation

AWG

American Wire Gauge

Chapter 1

Introduction

1.1 Context and motivations

Lithium-ion batteries are integral to various applications, including electric vehicles, grid storage systems, laptops, and other electronic devices. Given their widespread use, ensuring their safety and reliability is crucial. One of the critical attributes defining these batteries' effectiveness is their lifespan. In recent years, there has been a surge in research aimed at understanding the aging mechanisms of batteries. The goal is to develop predictive models that can accurately estimate the remaining useful life of battery cells, often determined by their capacity over repeated charge/discharge cycles.
The existing literature on this topic is extensive and can be broadly categorized into model-based and data-driven approaches. Model-based approaches often involve mathematical and computational models to simulate and predict battery behavior and degradation over time. These models are typically grounded in the fundamental principles of electrochemistry and physics that govern battery operation. On the other hand, data-driven approaches leverage the power of artificial intelligence and machine learning. These methods focus on extracting meaningful features from the data collected during battery operation to train models that can predict battery life. Data-driven models are known for their ability to handle complex, non-linear relationships. They are particularly useful when the underlying physical processes are poorly understood or too complex to model accurately. In this thesis, we examine two distinct lithium-ion batteries; one that is new and another that showcases signs of degradation. One of the primary objectives is to determine the number of charge and discharge cycles the used battery has experienced by correlating it with its observable performance degradation.

To achieve this, a series of experimental tests were devised. The initial phase

involved benchmarking the performance of the non-degraded battery. Critical parameters, such as charge capacity and discharge rates were recorded. This offered a baseline against which the degraded battery's performance could be compare. Building upon these insights, the latter part focused on the construction of a predictive model. The aim is to forecast the trajectory of battery performance degradation over its lifecycle. Such a tool is precious, especially in applications where battery reliability and longevity are crucial.

1.2 Objective and Methodology

To achieve the objectives of the thesis, the methodology employed starts with a comprehensive literature search focused on test benches for LiPo batteries that can determine discharge curves. We also evaluated commercial test benches for their capability to provide the essential components, sensors, and an integrated software system for recording experimental data.
Once the components were selected, the test station was set up, and specific test parameters were defined. These parameters included external temperature, voltage values at the beginning and end of the test, the discharge current value, and the sample rate. For the tests, we utilized a new battery, free from degradation effects, and a used battery, which was expected to show signs of degradation. Each test was conducted for four different discharge currents.

Using MATLAB, the experimental data were then compared and analyzed. The next step involved creating a model that could predict the number of cycles of the old battery. Simulink was employed to craft a battery discharge model that would describe the new battery's performance. Furthermore, a model of capacity degradation based on the number of cycles was implemented. By simulating various cycles, we aimed to determine at which cycle the new battery's performance would align with that of the old one. The goals of this thesis include:

- **Design and development of an experimental test bench for LiPo batteries:** a crucial aspect of this study is to gather accurate and consistent data on the battery's performance and health across diverse operational scenarios. For this purpose, a test bench will be conceptualized and assembled. This bench will simulate the real-world scenarios that Unmanned Aerial Vehicle (UAV) batteries encounter, covering aspects like charge-discharge cycles and voltage variations. Essential metrics such as current, voltage, capacity, and internal resistance will be monitored and recorded.

- **Formulation of a LiPo battery predictive model:** using the data derived from the testbed, a custom predictive model for LiPo batteries will be crafted. A central element in this phase is the establishment of a capacity degradation model.

- **Applying the predictive model to define the number of cycles:** using the predictive model a estimation of the number of cycles that the battery has gone through over 2 years will be conduct.

1.3 Current State Of The Art (SOTA)

In this chapter, we will present the scientific research on the degradation of lithium-ion batteries' performance. It is worth noting that there are few studies and scientific articles available for free on LiPo batteries. However, since their operation is almost identical, it is interesting to consider the extensive literature on lithium-ion batteries. We'll review the main papers we relayed for the development of the degradation model.

In the study "Characterization of the Degradation Process of Lithium ion Batteries when Discharged at Different Current Rates", the authors tested a Sony US18650 1.4 Ah Li-ion battery by cycling it at various discharge rates (1-C, 2-C, and 3-C) under a controlled ambient temperature. After 300 cycles, the battery's capacities decreased by 9.5%, 13.2%, and 16.9% at 1-C, 2-C, and 3-C discharge rates, respectively. Figure 1.1 illustrates the capacity fade, recorded every 50 cycles, with actual measurements connected by straight lines.

We can see that every degradation curve displayed in figure 1.1 follows an exponential decay pattern, irrespective of the associated C-rate. Inspired by this observation, the study employed MATLAB's Curve Fitting Tool to align a two-term exponential expression, $f(t) = ae^{bt} + ce^{dt}$ with the actual degradation data. Figure 1.2 illustrates both the collected data and the curve adjusted to fit this data.

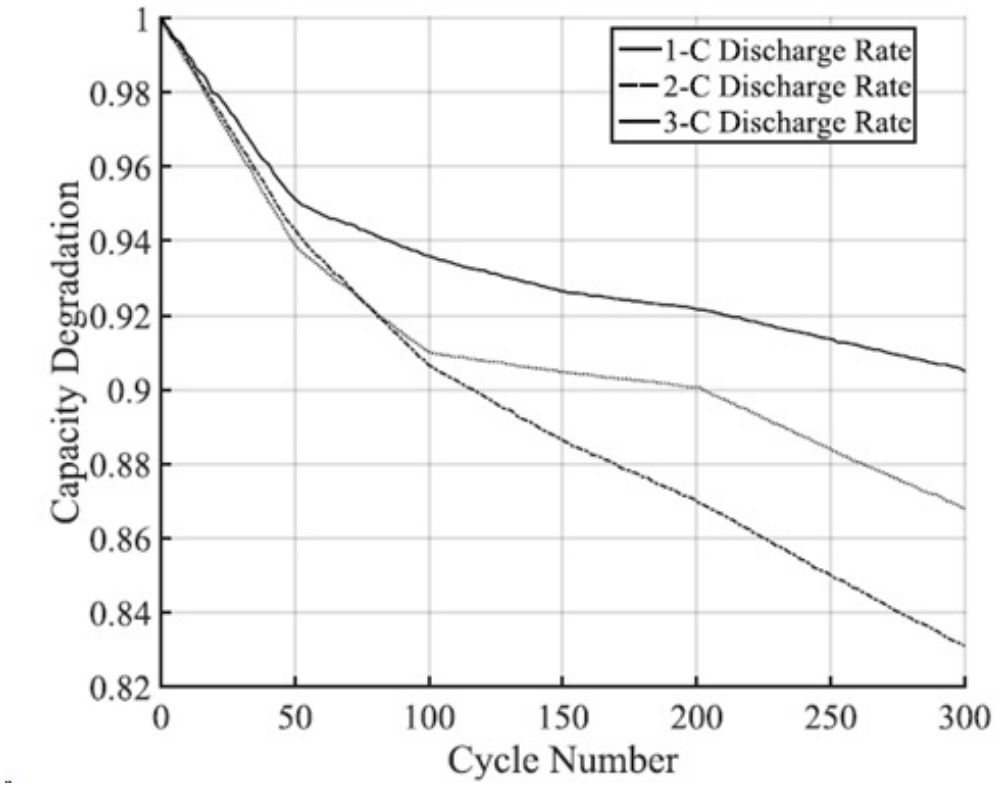

Figure 1.1: Capacity Degradation

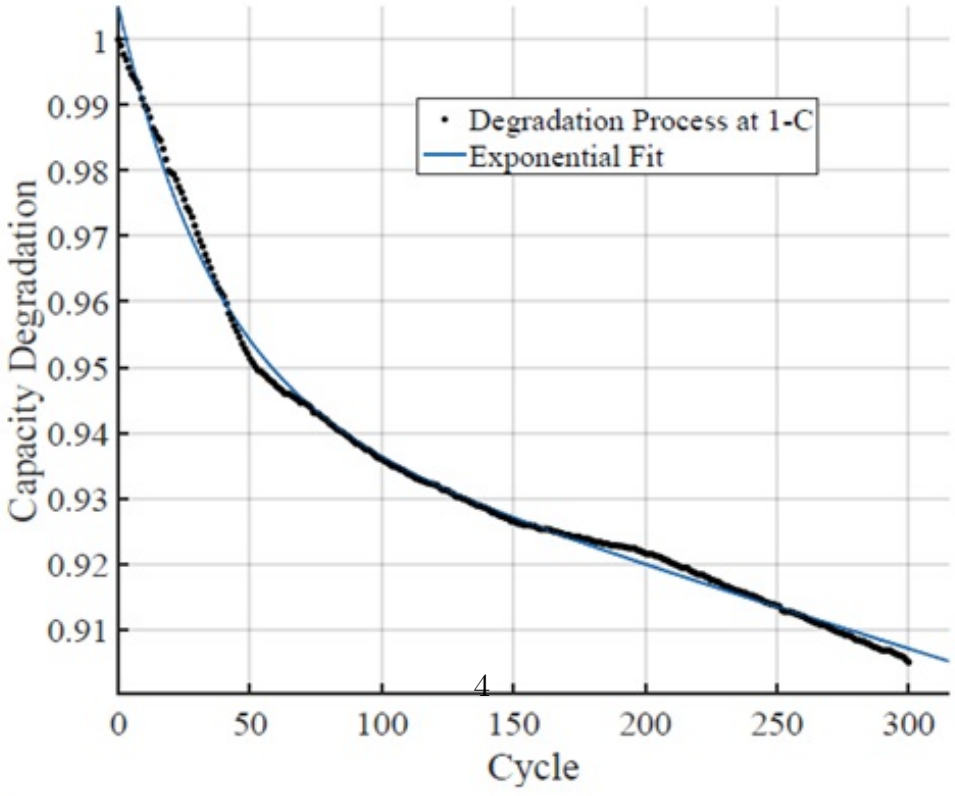

Figure 1.2: Degradation fitting curve

After that, the author calculates the coefficient of the fitting curve for every C-rate. The results are shown in figure 1.3.

Coefficient	Parameter	1-C	2-C	3-C
a	Mean Value	0.06108	0.07653	0.06763
	Confidence bounds	(0.06084, 0.06132)	(0.07371, 0.07965)	(0.06588, 0.06937)
b	Mean Value	-0.02905	-0.02896	-0.02093
	Confidence bounds	(-0.02931, -0.02879)	(-0.03165, -0.02627)	(-0.02203, -0.01984)
c	Mean Value	0.946	0.932	0.9376
	Confidence bounds	(0.9457, 0.9462)	(0.9292, 0.9349)	(0.9357, 0.9395)
d	Mean Value	-0.0001406	-0.0002115	-0.0003943
	Confidence bounds	(-0.0001416, -0.0001395)	(-0.000225, -0.000198)	(-0.0004026, -0.000386)

Figure 1.3: Coefficients

Finally, the study derives a C-rate dependent model for the degradation of SOH over time, where: $d = ae^{\beta(C-\text{rate})^2}$ is one of the coefficients of the previous relation. The average value and the confidence intervals for α and β are detailed in Figure 1.3. In this instance, the achieved R^2 value was 0.9997, indicating an excellent fit of the function to the data.

Parameter	α	β
Mean Value	8.93E-5	0.127
Confidence bounds	(6.94E-5, 1.09E-4)	(9.86E-2, 0.155)

Figure 1.4: Parameters

In the paper “Modeling long-term capacity degradation of lithium-ion batteries” The author experiment, detected a second bend when the capacity reached about 30% of its initial value. Consequently, the overall capacity degradation manifests an "S"-shaped or sigmoidal curve. Figure 1.5 incorporate the comprehensive data set gathered from the 48 cells tested in the study.

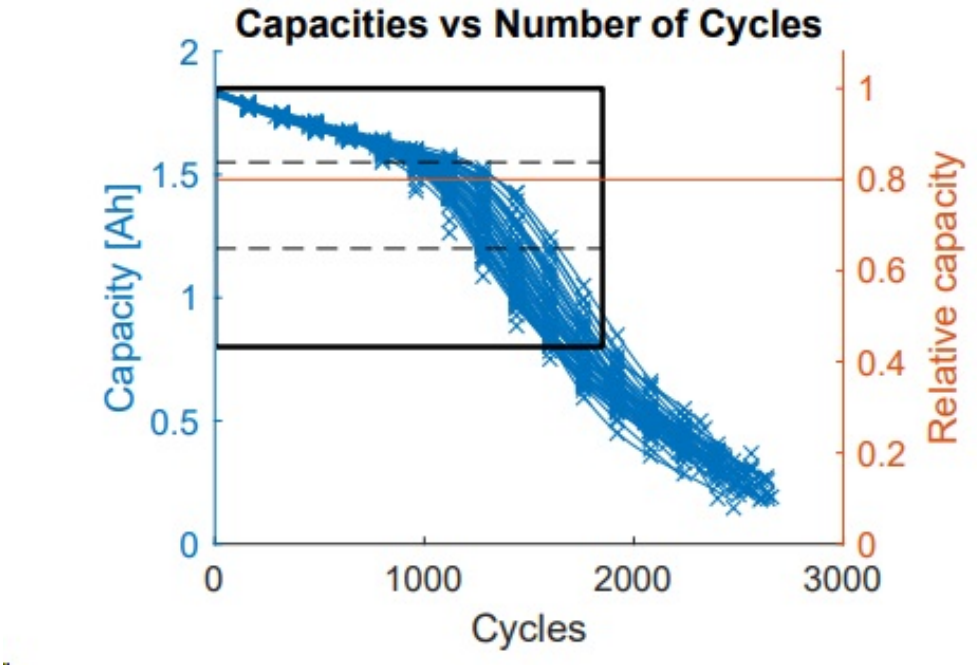

Figure 1.5: Different aging trends from 48 cells

To elevate the precision of the analysis, the author introduces a parametric regression model tailored to fit the specific battery data at hand. This model is not just a tool for curve fitting but is designed to mitigate the impact of measurement errors, enhancing the accuracy of the degradation analysis. It employs a stochastic approach, enabling the application of statistical procedures to refine the data interpretation further.
Each parameter within the model is not a statistical entity but is chosen with meaning, allowing for a understanding of the underlying degradation dynamics. In existing literature, various parametric models have been explored to estimate the remaining capacity, like double exponential model, polynomial model, mixture model and the author studies the differences and the best approaches.
Also, in the study is presented a lifetime prediction. For lithium-ion battery cells' long-term capacity degradation behavior under cyclic aging, they propose a parametric regression model with the regression function being a linear combination of a linear and a logistic function. They use a sigmoidal model that allows for interpretation of all its five parameters and shows high flexibility in fitting different kinds of capacity degradation paths.

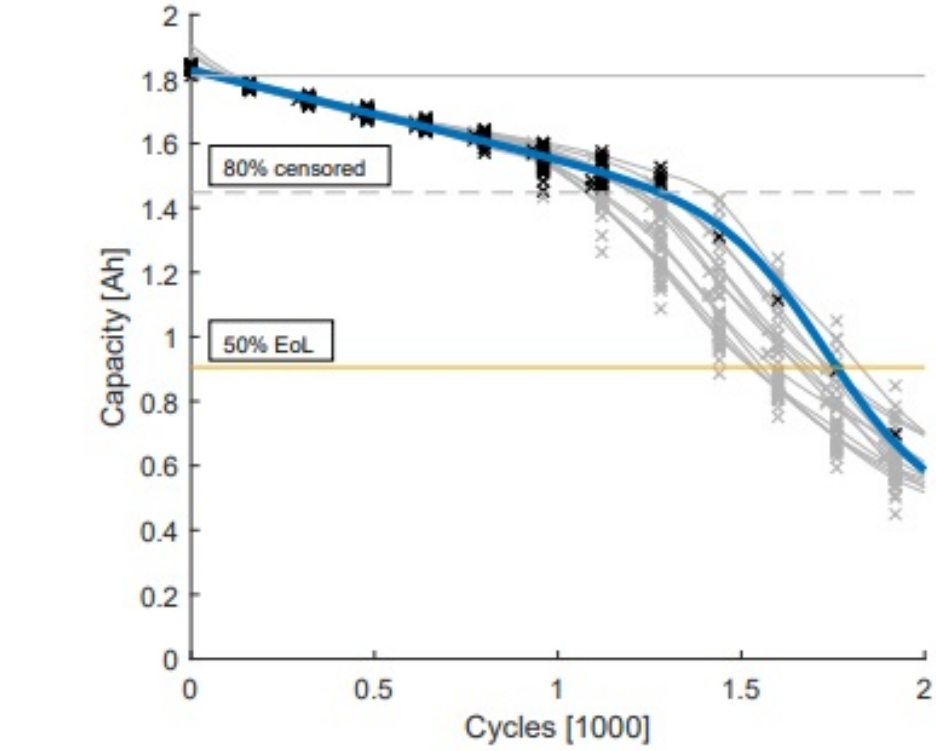

Figure 1.6: Long term capacity degradation

In the paper “Knees in Lithium-Ion Battery Aging Trajectories” the authors examine how various factors influence the "knee point" in battery degradation, classifying them into cell design, testing conditions, and sampling/testing variability. In terms of cell design, factors like electrode design, electrolyte composition, and formation protocols can impact the knee’s occurrence. Testing conditions, including charging and discharging rates and voltage limits, also play a significant role. The study reveals that higher charging rates and wider cycling voltage ranges typically accelerate the knee’s appearance, while the impact of discharging rates can vary. The authors emphasize the need for more research to understand these complex interactions and their effects on battery lifespan.

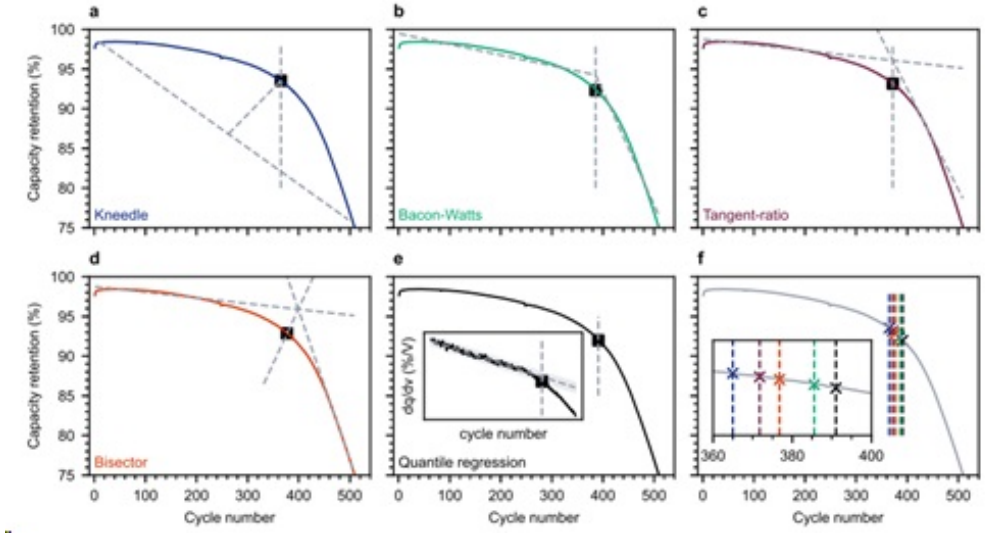

Figure 1.7: Results of various knee identification methods

Chapter 2

Technological background

2.1 LiPo batteries

Lithium-ion polymer (LiPo) batteries are powerful energy sources known for their high specific energy, high energy density, and slim, elongated designs. They are a variation of the standard lithium-ion battery but utilize a polymer gel as the electrolyte. Like their traditional counterparts, LiPos are rechargeable and deliver numerous high-energy discharge cycles. The operation of LiPo batteries involves the movement of lithium ions between the positive and negative electrodes, with a polymer gel electrolyte acting as the separator. Instead of a hard exterior, LiPo cells are usually encased in flexible pouches or wound prismatic.
This design allows for efficient packing during battery assembly and enhances heat dissipation. High-quality LiPo cells can achieve thousands of discharge cycles, making them suitable for space missions. The core specifications of a LiPo cell, such as voltage, energy, and power, are influenced by the materials used for the cathode, anode, and electrolyte. Commercially popular LiPos typically have a LiCoO2 cathode and a graphite anode. The polymer electrolytes in these batteries are gels infused with an ion-conductive salt like LiPF6.
Individual LiPo cells can be grouped in various arrangements. The most prevalent designs are the planar or stacked arrays, which often connect multiple cells in series to amplify the battery's voltage. For instance, a configuration with four cells in series is labeled as a 4s1p strand. When these arrays are connected in parallel, the battery's capacity increases, a standard planar battery setup with parallel connections might be described as 4s2p, where "s" indicates the number of series cells and "p" denotes the parallel strands. When battery packs are constructed using multiple cells, cell capacity has an inherent variation. This variation heightens the risk of cells undergoing harmful conditions like overcharging and overdischarging. This capacity disparity becomes more pronounced as the battery undergoes more

charge-discharge cycles, especially under extreme overcharge and overdischarge scenarios.
Issues like faulty cell connections or problematic charging circuits can result in overcharging, while circuitry leakage currents might cause overdischarging. Overcharging and overdischarging are the primary challenges faced by LiPo cells. Such mistreatment can lead to reduced performance (affecting the intended operation) or safety concerns. Every LiPo variant has a suggested voltage range determined by the specific chemistries of the cathode, anode, and electrolyte materials. This range defines the maximum and minimum voltage levels for safe operation.

The components of LiPo cells are:

- Aluminized Polyester Pouch is a tri-layered laminate packaging commonly used for LiPo cells. It consists of non-conductive polyester polymer layers on the outside and inside, with a central layer of impermeable aluminum foil.
- Aluminum foil serves as the metallic current collector, ensuring electrical contact from the positive electrode materials to the cell's terminal. Within the voltage range of the cathodic half-cell reaction, aluminum sustains a consistent passivation layer.
- Lithium cobalt oxide (LiCoO2) is a positive electrode material for lithium-ion and LiPo cells, especially in portable electronics. Its popularity stems from its high energy density, voltage, and cycling capability. The LiPo cells discussed in this report utilize the LiCoO2 positive electrode chemistry.
- The Separator is a micro-porous polymer membrane that electrically separates the electrodes but permits ionic conduction, ensuring electrical isolation between them.
- The Electrolyte salt, usually LiPF6, is an inorganic lithium salt that offers ionic conductivity and blends well with the electrolyte solvents.
- Electrolyte solvents are generally aprotic organic solvents that remain electrochemically stable within a voltage range of 0 to 5.0 V against Li.
- Graphite carbon (C) is the standard material for the negative electrode. It pairs well with LiCoO2 and other transition metal oxides and phosphate positives.
- Copper foil functions as the metallic current collector, facilitating electrical contact from the negative electrode materials to the cell terminal. Within the voltage range of the anodic half-cell reaction, copper maintains a stable passivation layer.

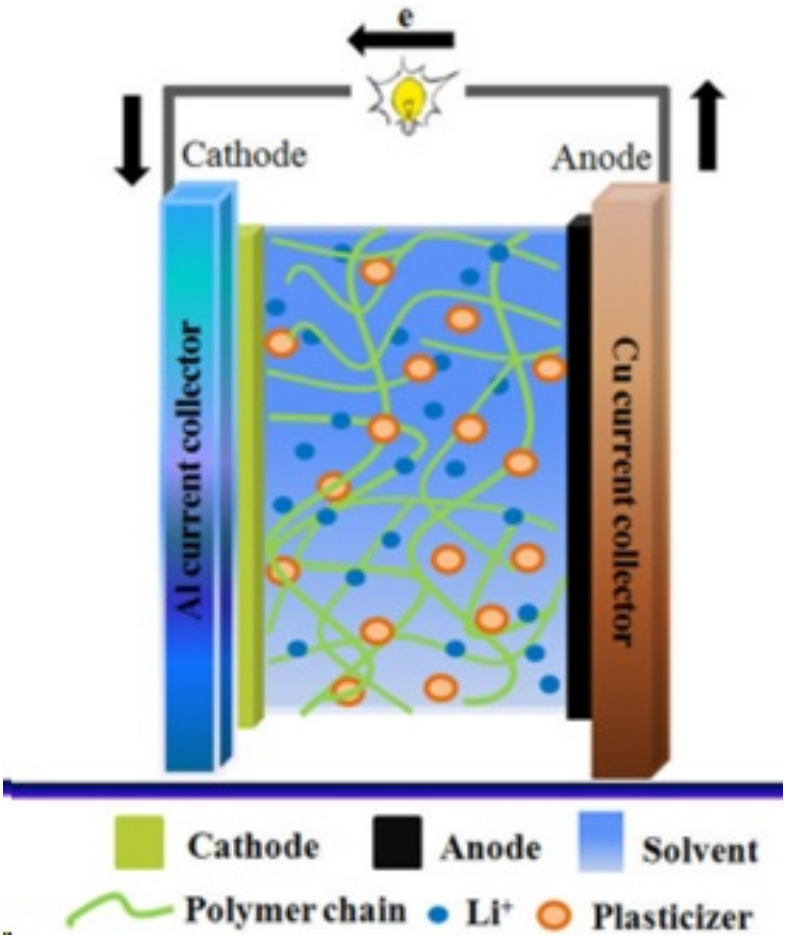

Figure 2.1: lipo technology

2.2 Battery diagnostics

Understanding the complexities of battery degradation is vital for optimizing energy. The longevity of LIBs is a focal point in reducing both costs and performance impacts. Over time, LIBs face reduced capacity and increased internal resistance due to various degradation mechanisms influenced by factors like temperature, state of charge, and load profile. We will overview these mechanisms and the conditions that trigger them. It highlights the role of external stress factors and secondary elements like manufacturing defects in influencing battery degradation.
As we said before, a standard battery consists of six primary elements. These include two current collectors in touch with the two electrodes, where redox reactions occur to facilitate the battery's charge and discharge processes. A porous separator is also present to prevent the electrodes from short-circuiting while enabling the

migration of charged ions. The electrolyte aids in easy charge transfer and serves as an additional source of lithium ions (Li+). These components are depicted schematically in Figure 2.2.

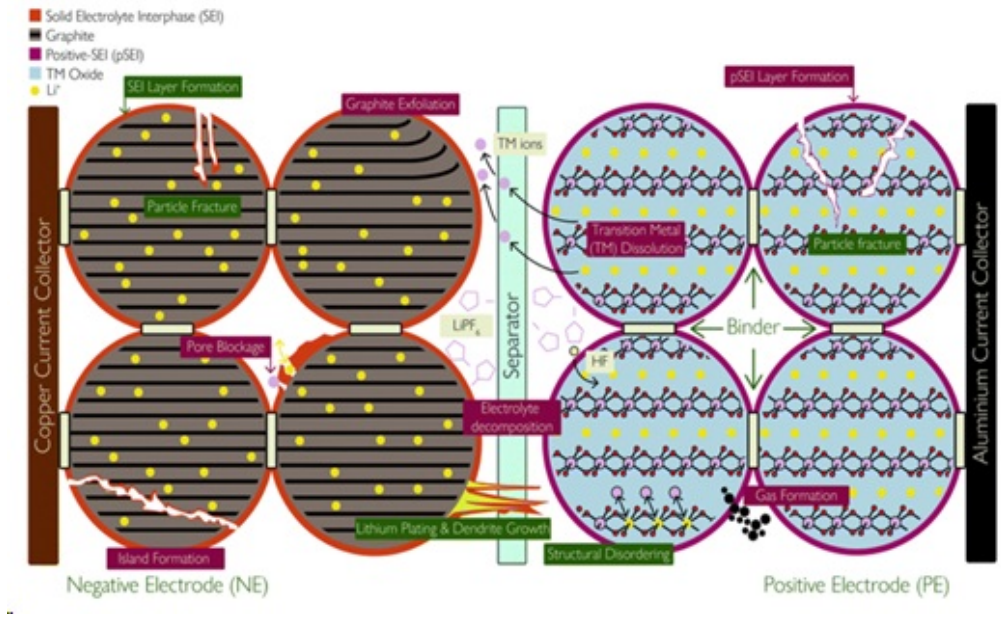

Figure 2.2: Schematic showing the basic components

The positive electrode (PE), typically made of lithium transition metal oxide, releases Li+ ions and electrons during charging. These ions move through the cell and separator to the negative electrode (NE), usually composed of graphite or similar materials, where they're accepted, maintaining charge neutrality. This "rocking chair" motion of ions and electrons reverses during discharge. The process's efficiency is tied to the ease of Li+ extraction from the PE and the stability of its crystal structure.

Battery degradation is a complex process. At the core, degradation mechanisms detail the physical and chemical changes occurring within the cell, though they are challenging to observe directly. These mechanisms lead to observable effects, namely capacity fade and power fade, which are easier to measure but offer a less detailed view of the degradation process. Bridging the gap between mechanisms and observable effects are degradation modes. These categorize the mechanisms based on their impact on the cell's behavior. Four key modes are highlighted: loss of active material (LAM), loss of lithium inventory (LLI), stoichiometric drift, and impedance change. LAM and LLI affect the cell's thermodynamic behavior, while impedance change, often referred to as resistance increase or impedance rise, impacts its kinetic behavior.

SEI Solid Electrolyte Interphase is a crucial component in the degradation of lithium-ion batteries. A passivation layer forms on the NE when the liquid electrolyte interacts with it. This typically occurs when the NE operates at voltages below the electrolyte's electrochemical stability window, leading to the irreversible breakdown of the electrolyte and its loss. SEI formation is a double-edged sword. Initially, it causes about a 10% reduction in battery capacity but then acts as a protective layer, preventing further electrolyte reaction with the NE. Over time, however, the SEI layer thickens, especially on graphite NEs, due to factors like solvent molecules diffusing through the existing SEI, exposure of new electrode surfaces from cracking, and deposition of side reaction products. The growth of the SEI layer is a natural process but can be accelerated by high temperatures and currents. Elevated temperatures increase diffusion rates, while high currents can lead to particle cracking and new SEI formation. The consequences of SEI growth are significant, leading to capacity loss, and increasing the cell's overall impedance, resulting in power fade. The SEI layer's reduced permeability to Li+ ions, pore blocking, and consumption of the electrolyte solvent exacerbate these effects. SEI growth is also linked to other degradation mechanisms. high cycling rates can cause particle and SEI cracking, exposing new surfaces for further SEI formation, and compounding the degradation process.

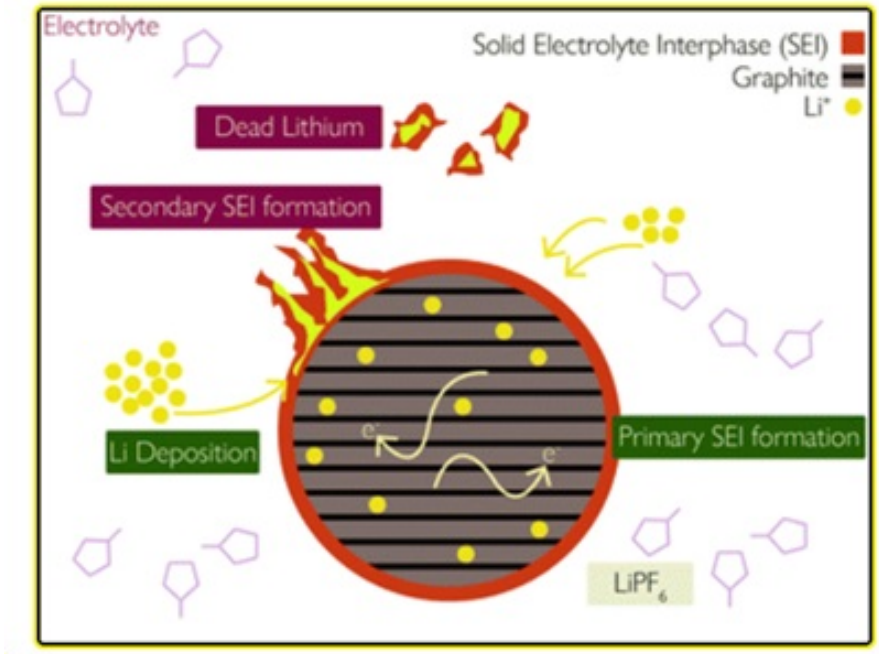

Figure 2.3: Interaction between SEI and lithium plating

Lithium plating occurs when metallic lithium forms on the surface of the NE instead of being absorbed into it. This phenomenon can be attributed to the NE surface being fully lithiated, leaving no room for additional lithium (thermodynamic plating), or due to rapid charging that increases the rate of this side reaction (kinetic plating). Lithium plating is particularly prevalent at low temperatures where the main lithium absorption process is slowed down. Several factors can exacerbate lithium plating, including low temperatures, high states of charge, rapid charging, high cell voltage, and an insufficient mass of NE or its electrochemically active surface area. To mitigate this issue, batteries are often designed with an extra 10-20% capacity in the NE to prevent overcharging. Additionally, an "overhang" or extra surface area is included to minimize local overcharging at the electrode edges. However, these measures could be more foolproof, especially during fast charging or in sub-freezing temperatures. Local defects in the separator or NE, whether originating from manufacturing errors or developing during use, can also lead to lithium plating. While calendar ageing is slow at low temperatures, indicating a reduced occurrence of lithium plating when the battery is at equilibrium, rest periods following fast charging can promote the reaction of plated lithium with the electrolyte over its removal by stripping.

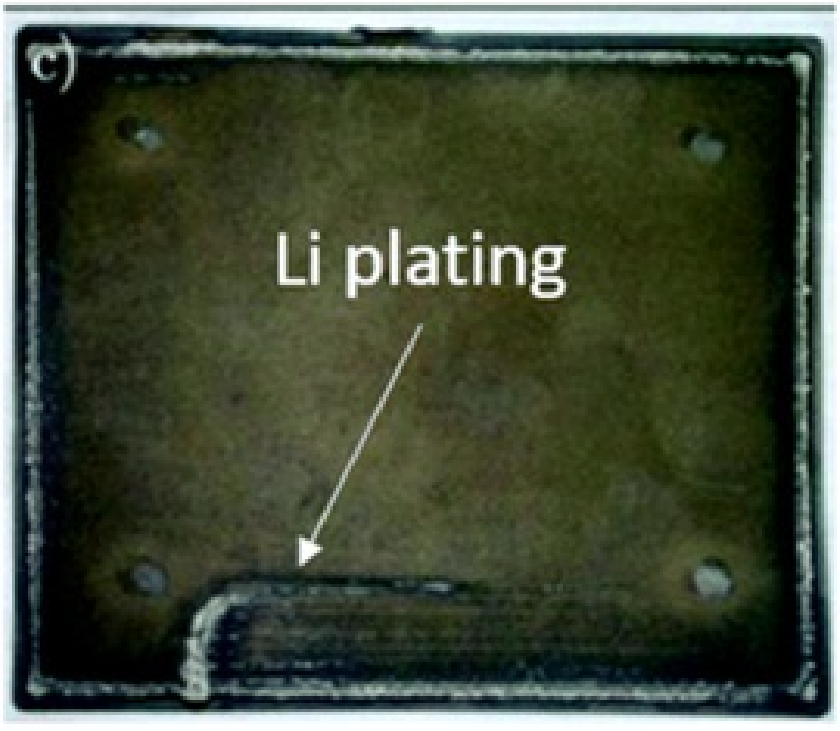

Figure 2.4: Graphite electrode after extensive Li plating

Particle fracture is a common issue in both electrodes of a battery, resulting from the significant volume changes and the ensuing stress during the battery's operation. This phenomenon is particularly pronounced near the separator, where higher local current densities lead to increased stress and, consequently, particle fragmentation. Materials with high theoretical specific capacity, such as silicon, are especially prone to particle fracture. The incorporation of silicon additives in electrode materials can substantially enhance their specific capacity. For instance, a pure silicon electrode can deliver a specific capacity over 11 times higher than its graphite counterpart. However, this increased capacity comes with the challenge of managing the pronounced volume changes and stress that silicon undergoes during the battery's charge and discharge cycles, leading to an increased propensity for particle fracture. Temperature extremes exacerbate particle fracture. Elevated temperatures increase thermal stress, while low temperatures make graphite more brittle and prone to fracture. Batteries with high silicon content NEs, subjected to deep discharge, high currents, or comprised of large particle sizes are particularly vulnerable. Manufacturing processes can also introduce strain effects and pre-existing cracks, accelerating particle fracture during battery operation. Cracks in electrode particles expose new surfaces to the liquid electrolytes, leading to side reactions and trapping of cyclable Li within the expanded SEI layer. The SEI layers, with distinct mechanical properties compared to active electrode materials, are more susceptible to cracking. NEs with high silicon content undergo significant volume changes during cycling, making them more vulnerable to particle cracking and associated SEI growth.

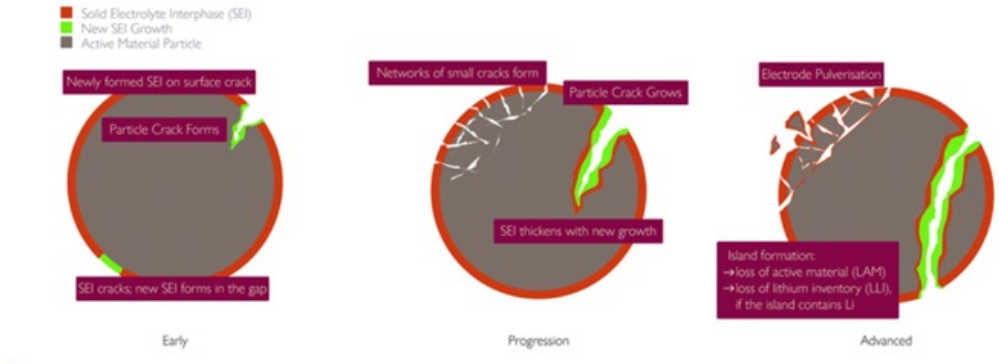

Figure 2.5: links between particle fracture and SEI growth

Chapter 3

Test bench development

In this chapter, we describe the development of the test bench capable of recording the battery's voltage and current data during the charging and discharging phase.

3.1 Test bench design

We must first establish our objectives and requirements to design the test bench accurately and functionally. The primary goals are as follows:

- The test bench should be able to measure the voltage, current, and power of a LiPo battery during the discharge phase.
- The measurements should be accurate.
- The measurements should not be affected by external temperature.
- The bench should be able to record the measured data.
- The bench should be able to discharge the battery using an external load.
- The battery should be able to be discharged at different currents.
- The data should be analyzable.

The aim is for the experimental data obtained to be as reliable as possible and the measurement error to be minimal. Moreover, knowing that the battery's performance is closely tied to the operating temperature, we must also consider the testing environment in the design to ensure that the experimental data is not dependent on external temperatures.

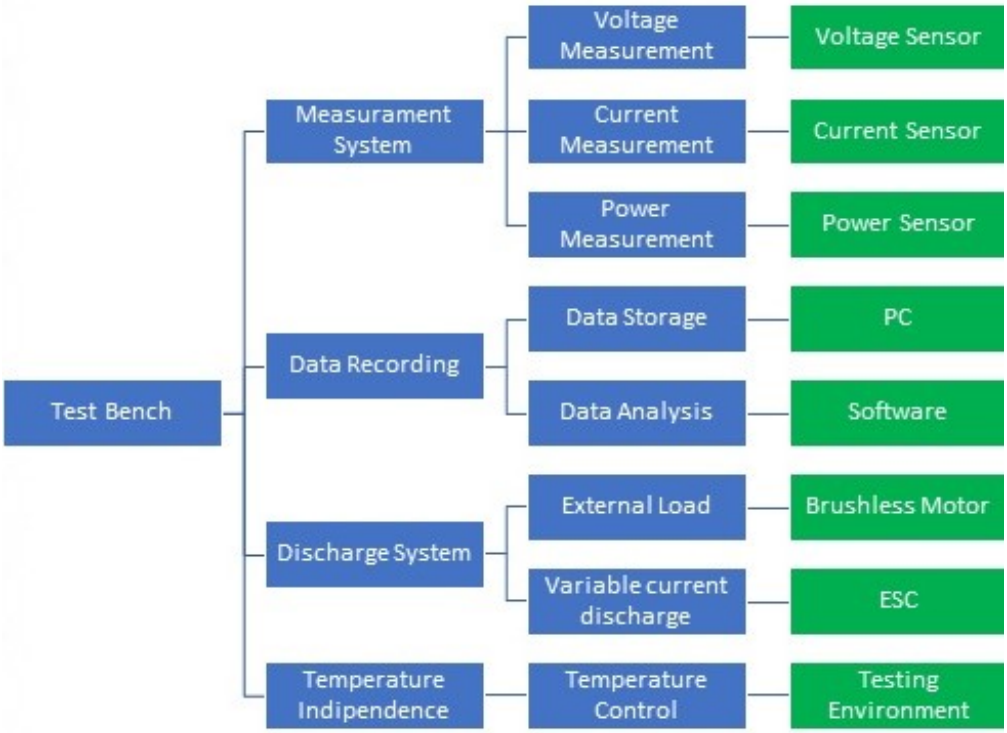

Figure 3.1: Functional tree

In the functional tree, we can observe the core functions of the test bench highlighted in blue, with the corresponding outputs marked in green. When it comes to measurement, we require sensors capable of detecting both voltage and current values. The power can then be computed by multiplying these two parameters.
For data management, a specialized software is essential, designed to analyze and store the data on a computer efficiently. We will employ an external resistance to discharge the battery, specifically utilizing a brushless motor. This choice aims to closely simulate a drone's mission, with an Electronic Speed Controller (ESC) to adjust the power accordingly. Lastly, the testing environment must maintain a consistent temperature throughout all tests to ensure the reliability and consistency of the data collected. This controlled environment ensures that the performance

and readings are not influenced by external temperature variations, guaranteeing the accuracy of our tests and findings.

Figure 3.2: Testbed Configuration

The final assembly of the test bench is depicted in Figure 3.2, showcasing its three core elements: the battery, the motor, and the computer. The motor support is fixed to a table with two screws, ensuring stability during operation, as illustrated in figure 3.3. The entire setup is housed in a laboratory room where the temperature is consistently maintained at 25 degrees Celsius, ensuring that all tests are conducted under uniform thermal conditions.
We procured the essential components from TytoRobotics, a company renowned for developing specialized test benches for evaluating drone performance and other related applications. TytoRobotics provided a electronic board equipped with the capability to manage various components and measure data. Accompanying this hardware is a software suite tailored for in-depth data scrutiny, ensuring that every piece of information is captured and analyzed.

Figure 3.3: Motor support and table fix

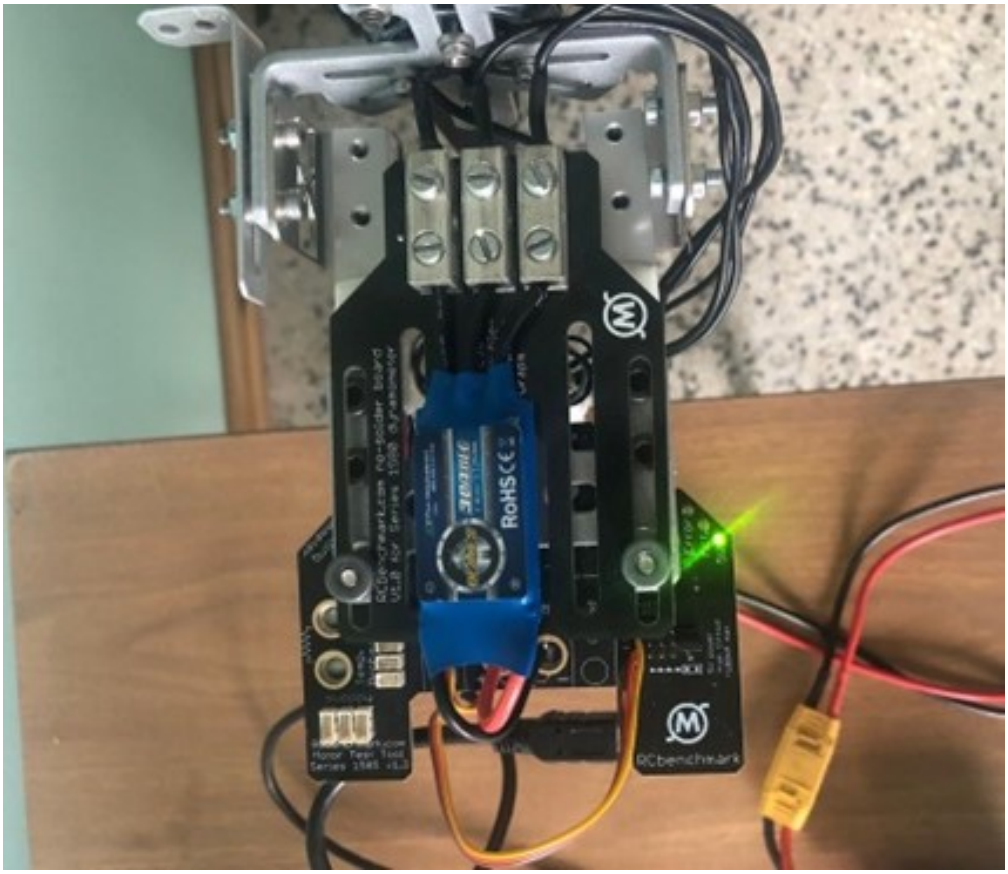

Figure 3.4: ESC link to motor and board

3.2 Component description

We provide an overview of the various components selected and assembled to create the test bench and the connections between them.

Figure 3.5: Lipo battery

The GENS product is equipped with a lithium battery that operates at a nominal voltage of 14.8 volts and is configured as 4S1P. It has a capacity of 6750mAh and uses an XT90-Plug connector. For our tests, we procured two of these batteries; one brand new and another that has been in use, to compare and analyze the variance in performance. The positive and negative wires of the batteries are connected directly to the printed circuit board (PCB).

Figure 3.6: ESC

The ESC serves as the intermediary between the battery and the electric motor, regulating the power flow and controlling the motor's rotational speed. It achieves this by converting the battery's direct current (DC) into a modulated three-phase alternating current (AC) through a sophisticated switching mechanism. This modulated AC, characterized by timed electric signals, dictates the speed variations of the motor. There are various protocols for delivering these signals, including PWM (Pulse Width Modulation), Oneshot, Multishot, and Dshot. Each has its unique characteristics, with the primary distinction being the frequency of signal delivery. A higher frequency results in faster signal transmission and, consequently, quicker response times for the drone. In our specific setup, we have opted for the PWM protocol. The ESC is connected to the PCB with two wires to secure the link for electrical signals, and to the brushless motor with the three wires to deliver the three-phase current.

Figure 3.7: PCB

The PCB for the RCbenchmark Series 1585 thrust stand is equipped with an array of features to enhance the functionality and versatility of the thrust stand. It includes an accelerometer for measuring acceleration and vibrations, and an ohmmeter with a range of 0.003 to 240 Ohms for resistance measurements. The PCB is designed with three connectors for load cells, enhancing its capability to measure forces accurately. It also features four PWM output ports for controlling and testing various motors and servos. For easy data transfer and connectivity, the PCB is equipped with a USB connector port. It supports power connections ranging from 0 to 50 V and up to 55 A, ensuring compatibility with a wide range of power sources. With a sample rate of up to 80 Hz for all sensors PCB ensures that data is captured with high precision and detail. The PCB is connected to both the ESC and the battery. This setup ensures that the ESC receives the power from the battery and effectively controls the motor's speed during the tests. Additionally, the PCB is connected to a computer that allows real-time observation of the data and that data is recorded.

Figure 3.8: Brushless motor

The T-Engine MN3508 380 KV is a brushless outrunner motor specifically designed for multicopters. This motor is characterized by its KV rating of 380, indicating the motor's RPM (Revolutions Per Minute) per volt that is applied, making it a suitable option for applications requiring moderate speed and torque. The motor features a 12N14P configuration. This denotes 12 stator slots and 14 magnet poles, a configuration that contributes to the motor's efficiency, performance, and smooth operation. To the motor we apply a propeller in order to create the resistance to discharge the battery.

Figure 3.9: Motor support

The mount in figure 3.9 is designed to hold the motor securely and offers great versatility. It allows for the easy attachment and removal of the motor, providing flexibility during testing or maintenance. Additionally, its adaptable design accommodates various types of motors, making it a universal solution for different motor models and sizes.

The mounts shown in figure 3.10 are used to secure the structure to a fixed component, which in this case is a table, and to attach the PCB and ESC firmly in place. These supports ensure stability and safety during the operation of the test bench, preventing any movement or vibration that could affect the accuracy of the tests or damage the equipment. The design allows for easy access to the PCB and ESC for monitoring, adjustments, or maintenance, ensuring that the test bench operates efficiently and reliably. It is crucial for the accurate data reading by the testbed to calibrate the structure. For this reason, an arm and weights are used, as seen in figures 3.11 and 3.12, which serve to calibrate the thrust of the motor. This process ensures that the measurements taken during the tests are precise and reliable, accounting for any potential discrepancies or biases in the setup. By carefully adjusting the setup with the help of the arm and weights, the testbed is optimized for accurate and consistent data collection, ensuring the validity of the test results.

Figure 3.10: Other supports

Figure 3.11: Arm component for calibration

Figure 3.12: Weights

Lastly, a decision was made regarding the use of cables. This aspect is crucial for ensuring the safety of the tests and avoiding the risk of burning the components. For this reason, the cables were sized by evaluating the maximum currents of each component and the operational currents. In our case, we chose an AWG 12, as shown in figure 3.13, to connect the battery and the ESC to the PCB. This choice ensures that the electrical connections are robust and safe, capable of handling the currents involved without overheating or compromising the integrity of the test setup.

Figure 3.13: Wires

3.3 Software implementation

The software of the RCbenchmark Series 1585 provides a simple and intuitive interface.

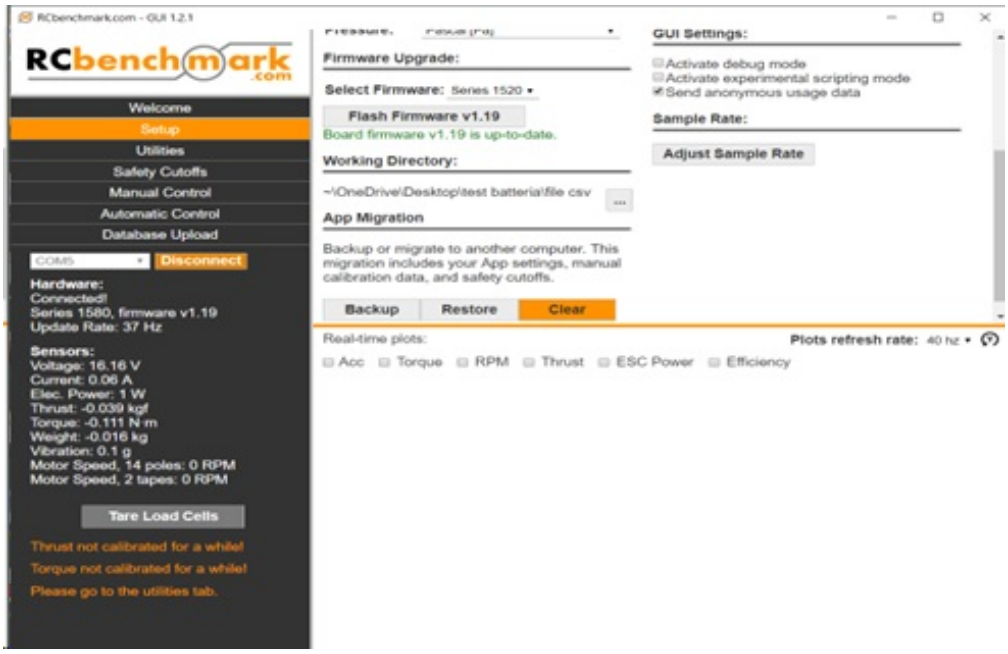

Figure 3.14: Tool interface

As we can observe in figure 3.14, on the left side of the screen, there is a menu for setup and control, which we will elaborate on later. Below this menu, there is a button for connecting the computer to the test bench via the COM5 port, and the text below it indicates the status of the connection. Following that, we can view the readings from various sensors on the test bench. In our case, we are particularly interested in the values of voltage, current, and electric power. On the right side of the screen, the display corresponds to the selected drop-down menu option.

As illustrated in figure 3.14, within the setup menu, it's crucial to define the PCB series for accurate data reading and set the working directory to ensure that the experimental data is directly saved to a specific folder on the computer. Another important parameter to set is the sample rate, which determines the frequency at which data is collected and recorded.
The maximum sample rate is limited by the hardware and driver settings. On most computers the tool is stable between 4 and 100Hz. the app is not capable of communicating with the driver settings, so you will need to modify the driver by hand. We'll choose a low sample rate if you want to perform extended datalogging.

For example, if you want to do an endurance test spanning multiple hours, you may set the sample rate at 4Hz to reduce the CSV data size.

The process of modifying the sample rate involves several steps:

1. Access the Windows Device Manager.

2. Identify and select the device that corresponds to the tool. This device should be associated with the same COM port that the app utilizes for communication with the board, as depicted in figure 3.15.

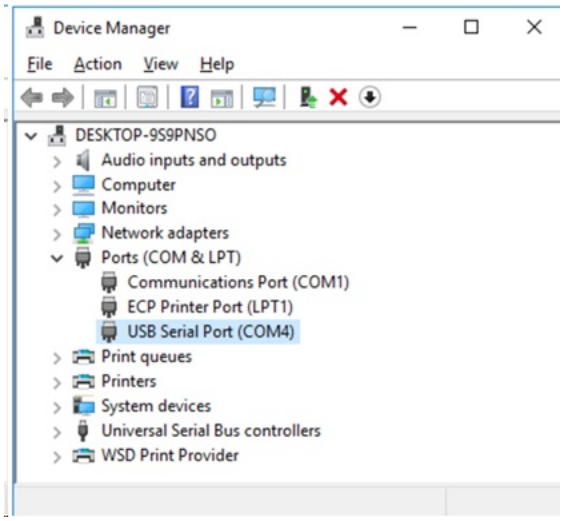

Figure 3.15: USB serial port

3. Proceed to click on the “Advanced...” option.

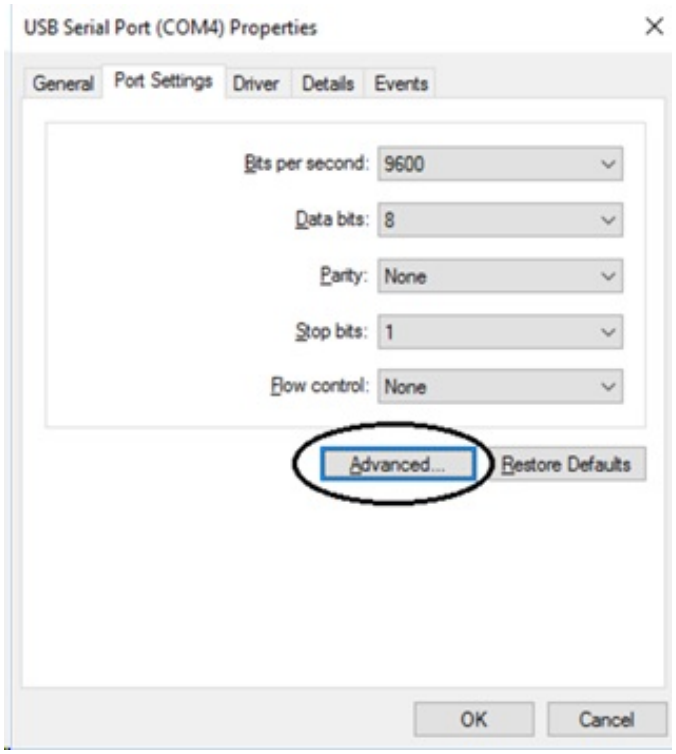

Figure 3.16: Port properties

4. The latency is expressed in milliseconds, and its conversion to Hz can be achieved using the formula: latency = 1000/Hz. Alternatively, the table in figure 3.18 provides a handy reference for this conversion.

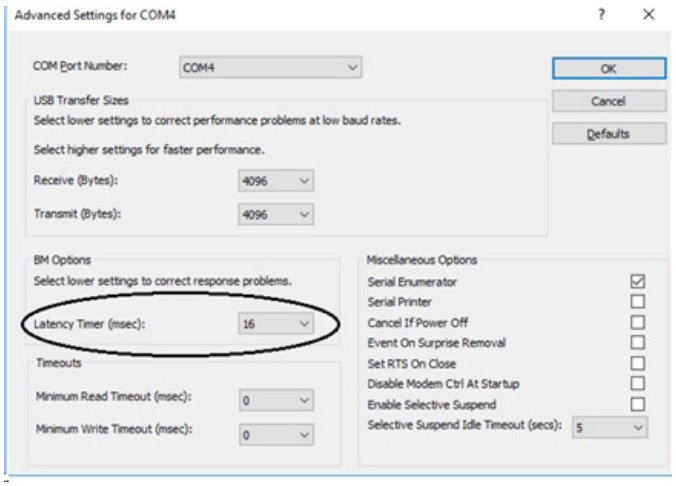

Figure 3.17: Latency Time

Latency Setting (ms)	Maximum Sample Rate (Hz)	
4	250	
10	100	
16	63	Default
20	50	
50	20	
75	13	
100	10	
125	8	
150	7	
200	5	
250	4	

Figure 3.18: Latency conversion

As we said we set 4Hz.

In the utilities menu, users can configure the PWM settings to ensure effective communication between the ESC and the PCB. This configuration is crucial for controlling the motor's power levels effectively. The power limits are defined within a range, with 1000 representing the point where the motor remains stationary, and 2000 indicating the motor operating at its maximum power. These numerical values are integral in calibrating the motor's operational range, ensuring it functions within the designated power limits to avoid potential damage or inefficiency.

Additionally, a safety cutoff feature is incorporated to enhance the safety and reliability of the testing process. If the system encounters a scenario where the operational parameters exceed the predefined safety thresholds, the tool automatically triggers the safety cutoff. In such an event, the ESC is instantly adjusted to a value of 1000. This response mechanism protects the motor and associated components from potential damage due to excessive power or operational anomalies.

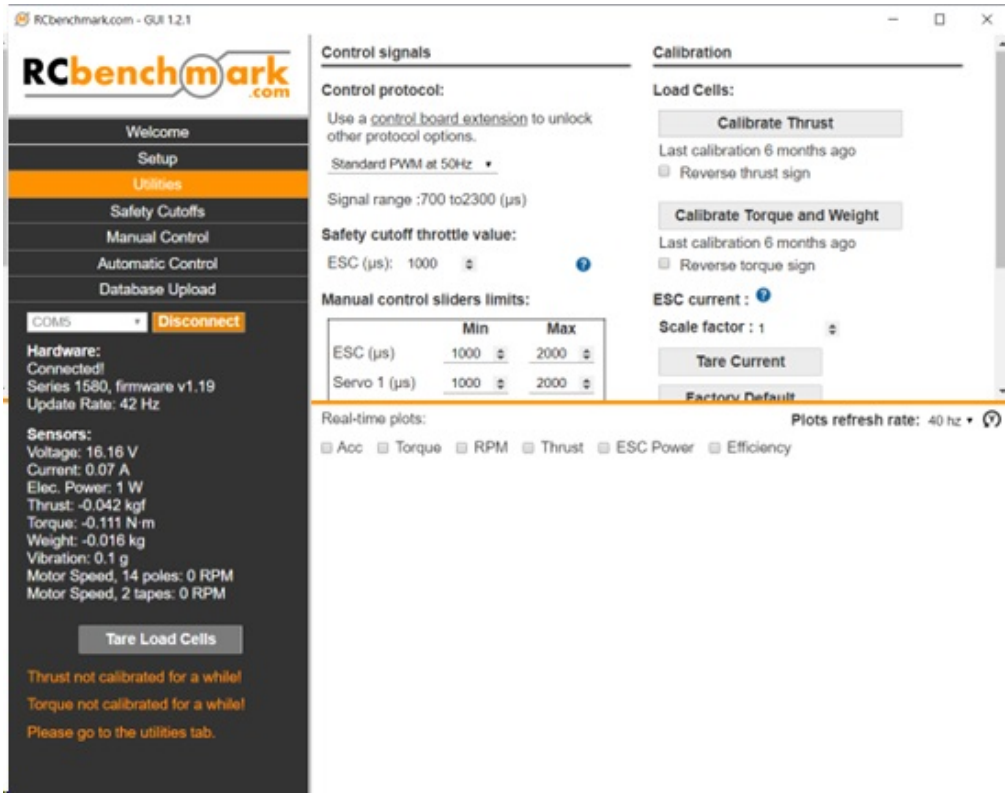

Figure 3.19: Utilities Menu

In the safety cutoffs menu in figure 3.20, users can establish the performance boundaries for the battery during testing, enhancing the safety protocols. This customization allows for a more controlled and secure testing environment, ensuring that the battery operates within the defined limits to prevent any potential hazards or damage. For our specific case, it is crucial to set the limits for voltage, current, power, and vibration to ensure the battery's safe operation during the testing phase. The voltage is configured with a maximum limit of 16.8 V and a minimum threshold of 14.5 V. This range ensures that the battery operates within optimal voltage levels, preventing overcharging or excessive discharge, which could potentially harm the battery's lifespan and performance. The current is capped at a maximum of 14.4 A, ensuring that the flow of electric charge remains within safe levels to avoid overheating or other potential issues related to excessive current. Electrical power is another critical parameter, and it is set to a maximum limit of 350 W. Vibration is also monitored and controlled, with a maximum allowable limit set at 2.5 g. This limit ensures that the battery and associated components are not subjected to excessive vibrations, which could lead to mechanical failures or affect the integrity of the connections and components.

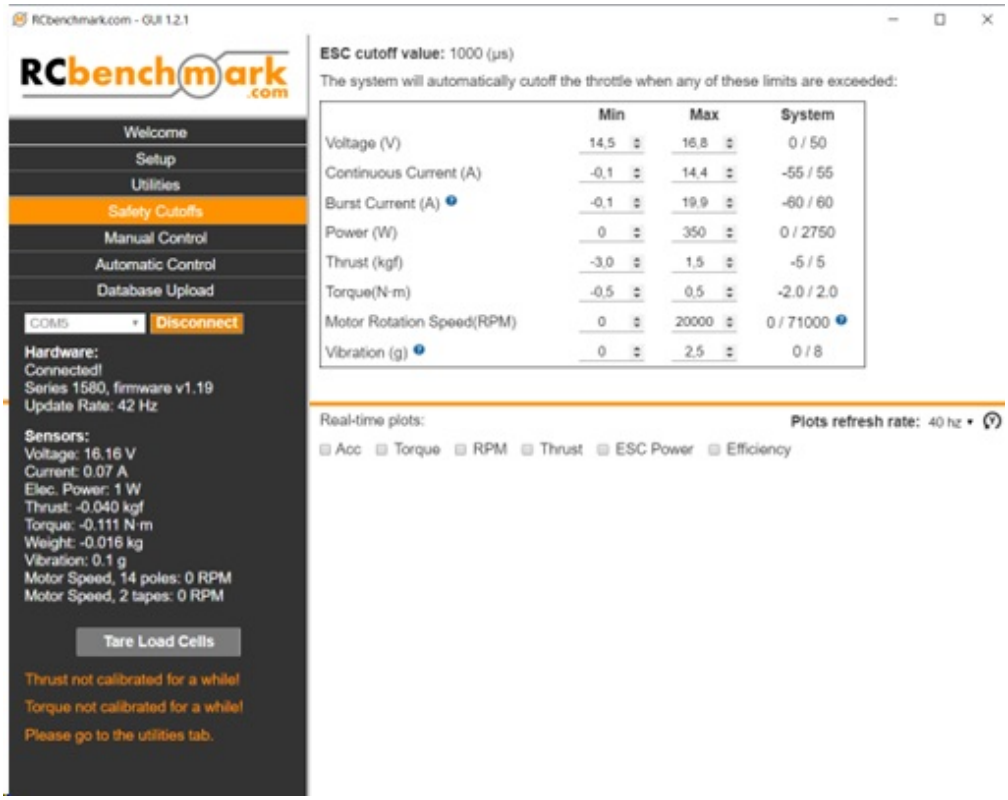

Figure 3.20: Safety Cutoffs Menu

In the manual control menu, users can directly control the motor's power level using the ESC slider. This feature provides a hands-on approach to adjusting the motor's power output, offering precise control over the discharge current level. Users can easily slide the controller to a specific position, setting a constant discharge current that will be maintained throughout the entire test. One of the key features in this menu is the continuous recording button. When activated, this function initiates the data recording process, capturing real-time data on the battery's performance metrics. All the collected data is saved directly to a CSV file. The file is stored in the pre-defined working directory, streamlining the data management process and ensuring that all test data is organized and readily accessible for review and analysis.

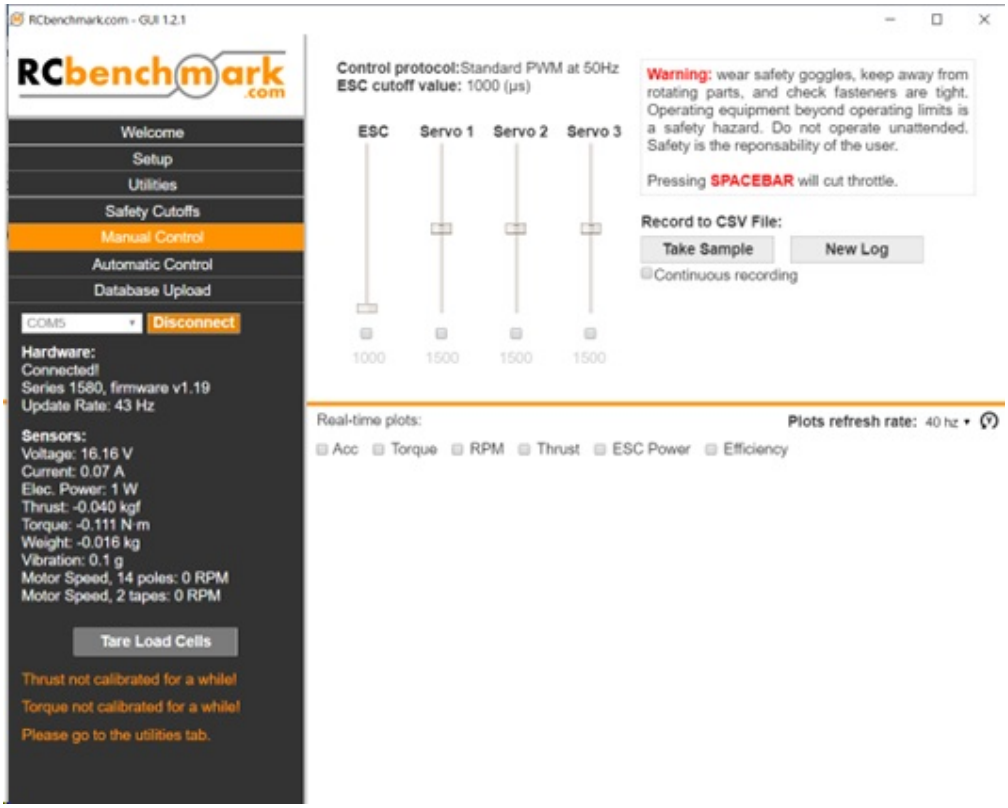

Figure 3.21: Manual Control Menu

Chapter 4

Experimental tests

4.1 Experimental testing methodology

The methodology employed for conducting the tests involves several steps. A fundamental prerequisite is maintaining identical experimental conditions for both the new and old batteries. This uniformity is crucial to ensure a reliable comparison of the performance metrics. The testing process commences with the new battery. It will be tested at various C-rates, specifically at 0.5C, 0.7C, 1C, and 1.2C. Each test initiates at a voltage of 16.3 and concludes when the voltage drops to 14.5. This range ensures a comprehensive assessment of the battery's performance under different discharge rates, offering insights into its efficiency and endurance.
Data management is integral to the testing process. Each set of data saved in the folder will be renamed to avoid confusion and ensure orderly storage. The naming structure will be systematic: it will indicate whether the battery is old or new, specify the C-rate, and number the test.
For instance, a name might read "new_0.5C_test1." This meticulous approach to data naming ensures easy retrieval and analysis. Redundancy is built into the testing methodology to account for any inadvertent or random errors. Two tests will be conducted at each C-rate, ensuring that any anomalies can be identified and accounted for, enhancing the reliability of the results.
Following the completion of tests on the new battery, the old battery will undergo the same testing regimen. Throughout the testing process, the room temperature will be meticulously maintained at 25 degrees Celsius. This constant temperature ensures that external thermal factors do not influence the batteries' performance, ensuring that the derived data truly reflects of the batteries' inherent capabilities and characteristics.

4.2 Description of performed tests

As observed in the figure 4.1, the experimental test curves exhibit a decreasing trend of voltage over time. The dynamic behavior of the voltage varies according to the discharge current. Specifically, the voltage decreases more rapidly with higher discharge currents, reaching the lower limit of 14.5 V in a shorter time. One initial observation is the distinct discharge times of the battery at different discharge currents.

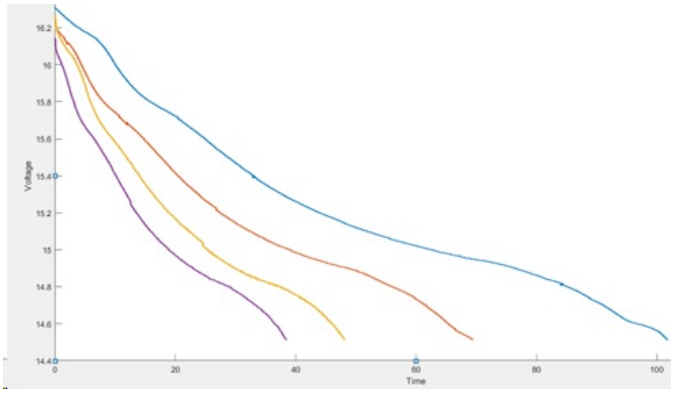

Figure 4.1: Discharge curves

A notable aspect of the conducted tests is the significant drop in voltage at the onset of the test when the external load is applied. This drop is more pronounced at higher C-rates. A similar behavior is observed at the end of the test when the external load is removed, resulting in a slight increase in voltage. This phenomenon is attributed to the internal resistance of the battery, where a voltage drop occurs, and is more significant with higher currents. Consequently, the voltage read by the external load is the battery's voltage minus the voltage drop across the internal resistance.

Given that the thesis aims to develop a predictive model of the battery capacity based on the number of cycles, one approach could be to calculate the trend of internal resistance and its degradation as a function of the number of cycles. However, this approach is complex, as we know that battery performance degradation is not solely dependent on internal resistance. It is influenced by various factors, including the degradation of internal battery components and electrochemical processes. Therefore, a preferred approach is to consider a model where all these factors are generally accounted for in the overall battery's capacity degradation. This comprehensive approach ensures a more accurate and holistic understanding of the battery's performance and degradation patterns over time and usage cycles.

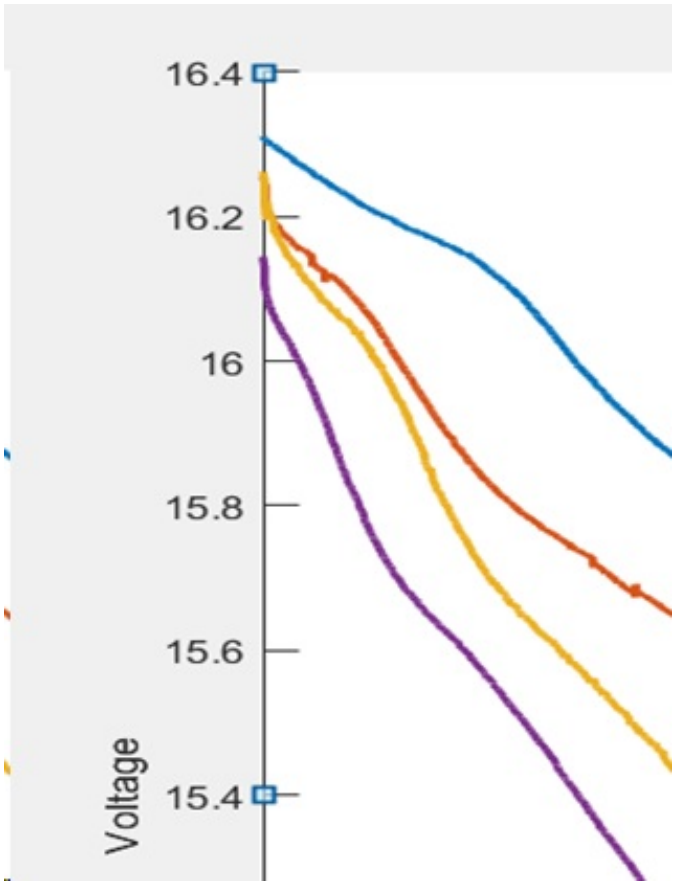

Figure 4.2: Initial Voltage Drop

4.3 Analysis of test results

Upon examining the discharge curves, it's evident that higher C-rates result in reduced battery autonomy. The curves showcase a sharp decline at the beginning of the test, followed by a more prolonged and steady behavior between 15.7 and 14.8 V, which represents the battery's optimal operating range. Towards the end of the discharge, there's a noticeable "knee" or inflection point, indicating the onset of a rapid voltage drop. Discharging the battery beyond this point could lead to potential damage, which is why we've set a safe threshold at 14.5 V.

Figures 4.3 and 4.4 depict the discharge curves for the different C-rates of both the new and aged batteries. By comparing the discharge duration (represented in minutes on the x-axis), it's clear that the aged battery's autonomy is diminished compared to the new one, signifying degradation. This observation is crucial as it's not an obvious outcome and provides valuable insights for the continuation of

our study. The next step in our research will involve a thorough analysis of the collected data. We aim to discern patterns and establish relationships between the observed differences in the performance of the new and aged batteries. This will further our understanding of battery degradation and its implications on overall performance.

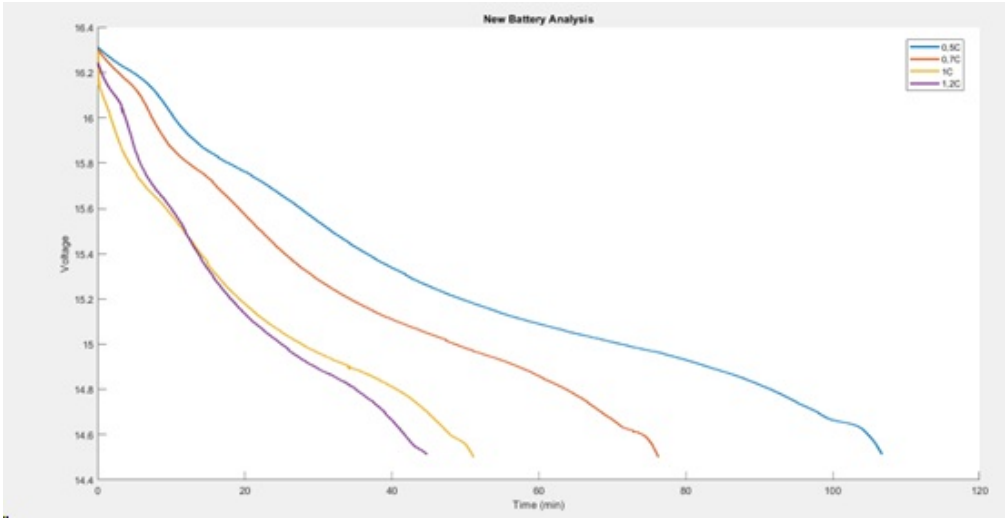

Figure 4.3: New battery discharge curves

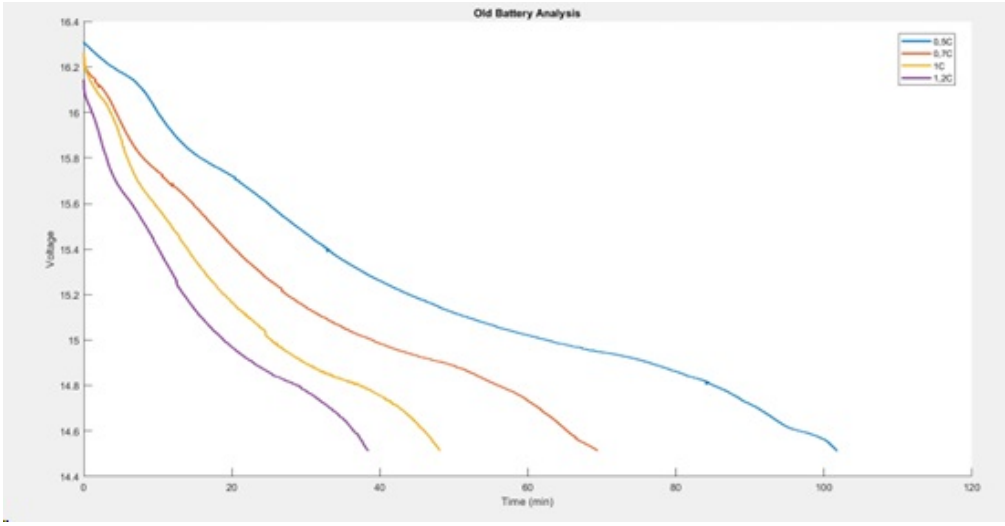

Figure 4.4: Old battery discharge curves

In figure 4.5, we can observe the capacity loss as a function of different C-rates. As evident from the graph, the capacity loss is more pronounced at higher C-rates.

This indicates that at elevated discharge currents, the battery experiences a more significant impact on its degradation. The performance deterioration becomes more pronounced as the current increases, highlighting the relationship between C-rate and the rate of battery degradation.

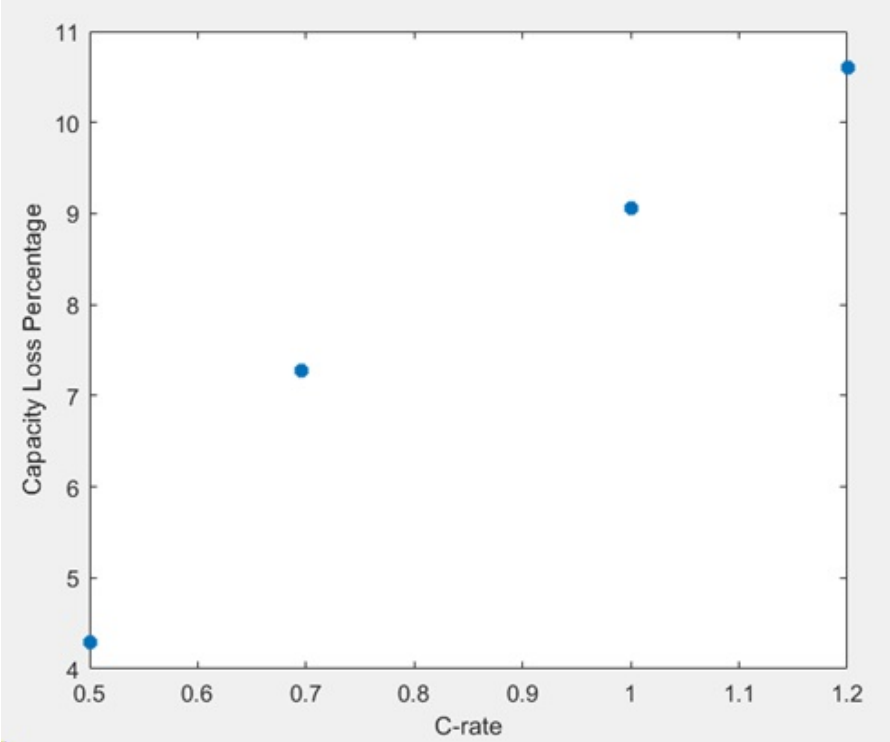

Figure 4.5: Capacity loss percentage

Chapter 5

Battery predictive model

5.1 Model description

After completing the experimental data collection campaign, the next goal is to process this data and develop a model that simulates the data trends. We have chosen to use MATLAB Simulink for this purpose. Simulink offers the capability to create models using blocks and their interconnections, providing a visual and intuitive approach to complex system modeling.
We opted not to use Simscape because this approach would have required specific data that we do not currently possess to accurately model the battery's discharge process. Instead, we constructed a high-level model capable of simulating the dynamic behavior of the voltage over time. In this model, we focus on capturing the essential characteristics and behaviors observed in the experimental data without delving into the intricate details that would require more extensive data and complex modeling. This approach allows us to achieve a balance between model accuracy and complexity, ensuring that the model is both representative and manageable.
Through Simulink, we can iteratively refine and validate our model, comparing its outputs with the experimental data to ensure alignment and accuracy. This iterative process facilitates ongoing improvement and refinement, ensuring that the model remains aligned with observed behaviors and can reliably predict the battery's performance under various conditions. In figure 5.1, we observe the battery discharge model. I will proceed to explain the significance of the block diagram. Each block and connection in the diagram represent a specific component or process involved in the battery's discharge, and together, they provide a comprehensive overview of the entire discharge process. The blocks are configured and parameterized to mirror the real-world behavior of the battery as closely as possible, based on the collected experimental data.

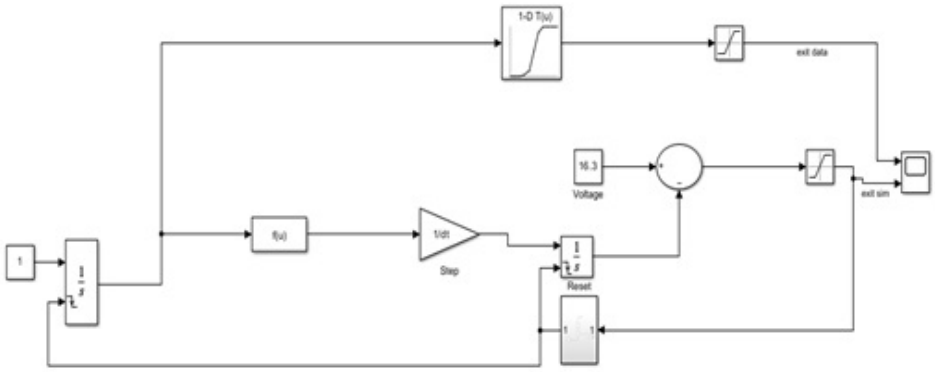

Figure 5.1: Discharge Model

Starting from the beginning, we can see a constant block. The goal here is to simulate the passage of time, and this can be achieved using a constant block and an integral block. In this setup, the integral block takes the constant one and multiplies it by the chosen integration step. The selection of the integration step is crucial. In our case, the choice was dictated by the sample rate of the experimental data, which defined the value of time and the corresponding voltage data. By using an inherent integration step, we have the opportunity, through a lookup table block, to display the experimental data in a scope block.
The lookup table block is configured with the experimental data, mapping each time step to the corresponding voltage value. As the simulation progresses, the integral block effectively 'counts' the time steps, and for each step, the lookup table block outputs the voltage value that corresponds to that particular moment in time.
This setup allows for a real-time display of the experimental data in the scope block, providing a visual representation of the battery's voltage over time, as per the collected data.

Regarding the simulation parameters, we opted to use a fixed step, given that the sample rate is constant, with the ode4 solver. The step size is set at 0.00007527. This choice ensures that the simulation closely follows the experimental data. The ode4 solver, also known as the Runge-Kutta method, offers a good balance between accuracy and computational efficiency. It's a widely used numerical method for solving ordinary differential equations, making it a suitable choice for this simulation where precision and performance are paramount. By aligning the fixed step size with the constant sample rate of the experimental data, we ensure that each simulation step corresponds directly to a data point from the experiment.

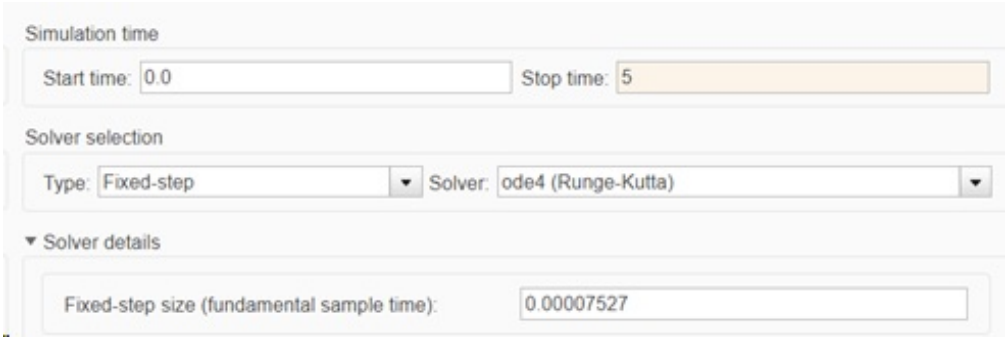

Figure 5.2: Solver Parameters

In the integral block, we set an external reset of the falling type. This configuration ensures that the integral resets each time a specific condition is met, which we will explain further ahead. By doing this, we can simulate multiple discharge cycles effectively. This approach is crucial for analyzing the battery's performance over successive discharge cycles. Each reset signifies the beginning of a new discharge cycle. The falling type reset is triggered when the signal transitions from a high to a low state, marking the end of one cycle and the commencement of the next.

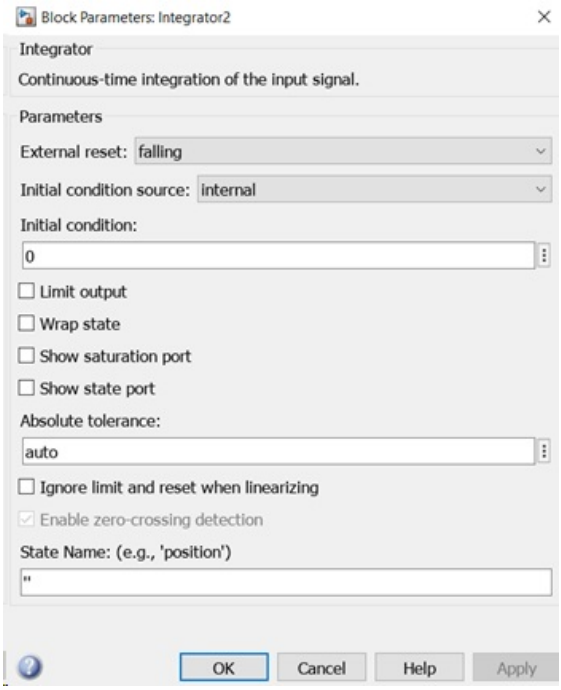

Figure 5.3: Integral Block

Moving on to the simulated model, we have time as an input to a function block where I have inserted a function that describes the discharge behavior of the voltage. To achieve this, I utilized MATLAB's 'diff' command on the experimental data file and fitted the behavior with a polynomial function.
In this context, the 'diff' command is used to compute the difference between successive elements of the experimental data, giving us a detailed view of the voltage's rate of change over time. This data is crucial for understanding the battery's discharge characteristics. The polynomial function is then employed to fit this differentiated data, providing a mathematical model that encapsulates the battery's discharge dynamics. By integrating this polynomial function into the function block, the simulation becomes capable of replicating the discharge patterns observed in the experimental data.

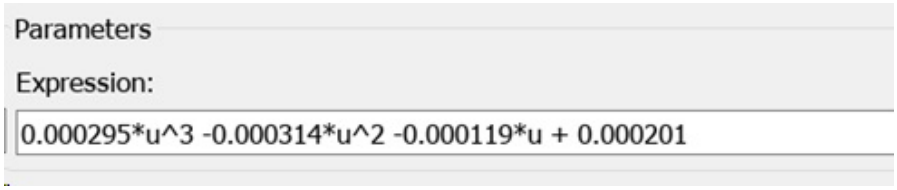

Figure 5.4: Function Block

In figure 5.5, as illustrated, I divided the output of the function by the integration step. This approach ensures that the integrator performs a cumulative summation. This process of scaling and integration convert the rate of change data into a cumulative representation of the battery's voltage over time.

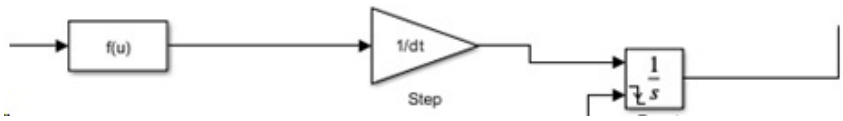

Figure 5.5: Cumulative Voltage Process

The previous output is then subtracted from a constant block set at 16.3, which represents the initial voltage value. This operation calculates the drop in voltage over time, providing a dynamic representation of the battery's discharge process. The resulting value, which signifies the real-time voltage of the battery, is then passed through a saturation block. This block is configured to limit the output values within the specified upper and lower bounds of 16.3 and 14.5 volts, respectively. These bounds correspond to the initial and final voltage values observed during the battery's discharge cycle. The saturation block ensures that the simulated voltage values remain within the realistic operational range of the battery. It prevents any potential overshoot or undershoot that might occur due

to the inherent approximations and assumptions embedded within the simulation model.

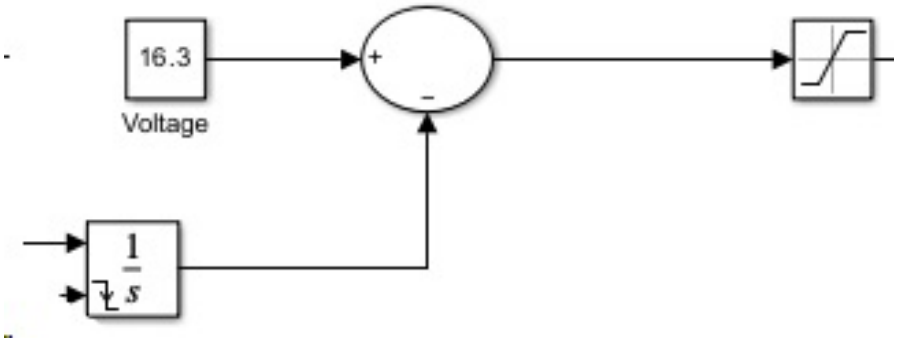

Figure 5.6: Battery's discharge process

So, the complete model of the simulated system appears as shown in figure 5.7.

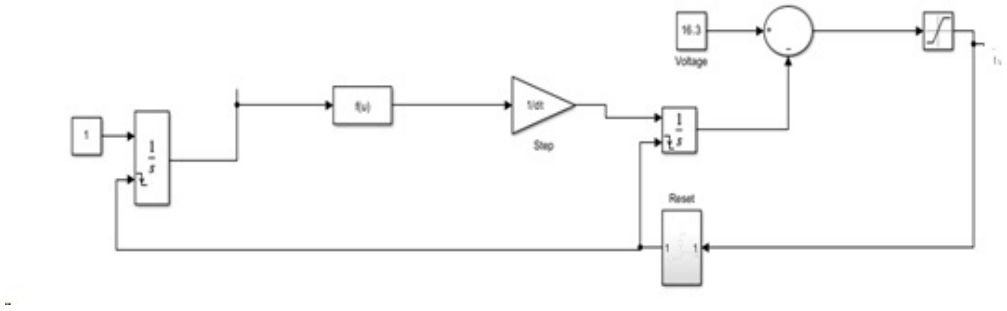

Figure 5.7: Simulation Model

The final block of the model is represented by a subsystem, as depicted in figure 5.8. This subsystem reset the integrators within the block diagram, enabling the simulation of multiple discharge cycles. Inside this subsystem, the output voltage from the global model is continuously compared to a constant value of 14.5 volts. This constant represents the end-of-discharge voltage, a critical parameter in battery performance analysis. As the simulation progresses and the battery discharges, the moment the output voltage matches 14.5 volts signifies the completion of a discharge cycle. At this juncture, the comparison yields a zero, indicating the battery has reached its lower voltage limit. This transition from a positive value to zero triggers the 'falling' type reset of the integrators. This mechanism ensures that the model can simulate multiple cycles seamlessly, offering insights into the battery's performance over repeated discharges.

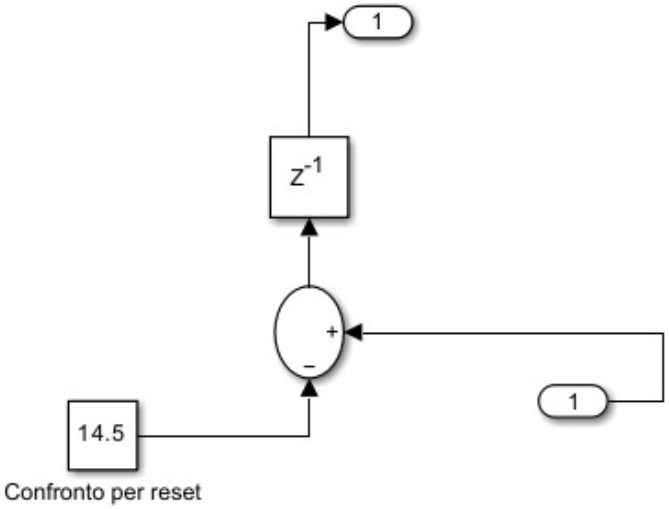

Figure 5.8: Reset Subsystem

With the Scope block, we can visualize the results of the simulation. Specifically, it allows us to compare the simulated model's output with the experimental data, enabling us to verify the correspondence between the two curves. This comparative analysis is crucial to validate the accuracy and reliability of the simulation model. Below, we present the results for the four different C-rates adopted in the simulation.

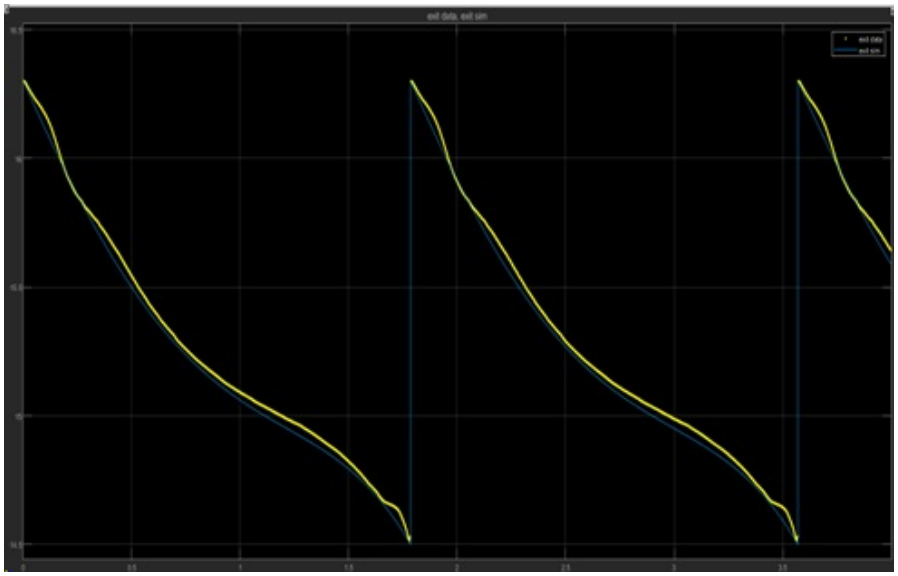

Figure 5.9: Simulation at 0.5C

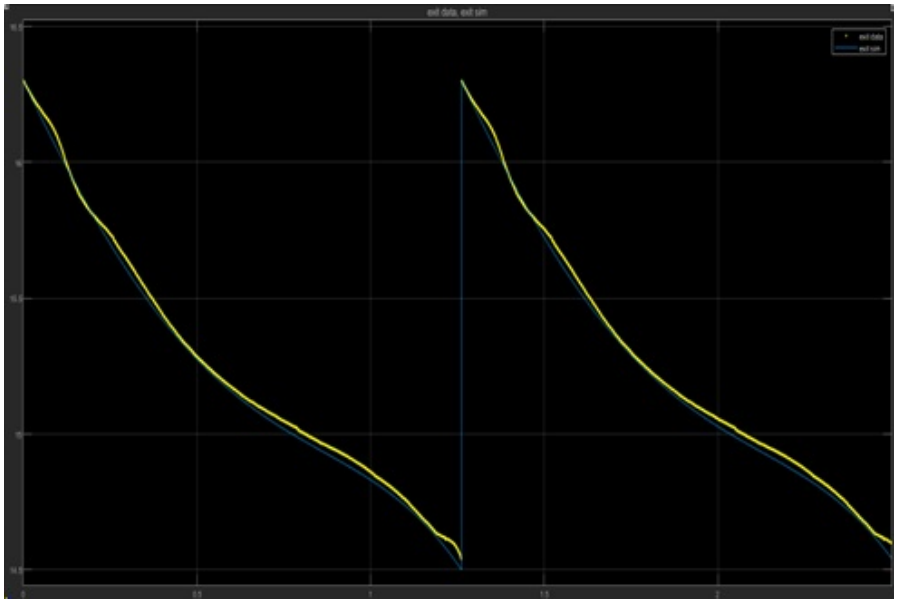

Figure 5.10: Simulation at 0.7C

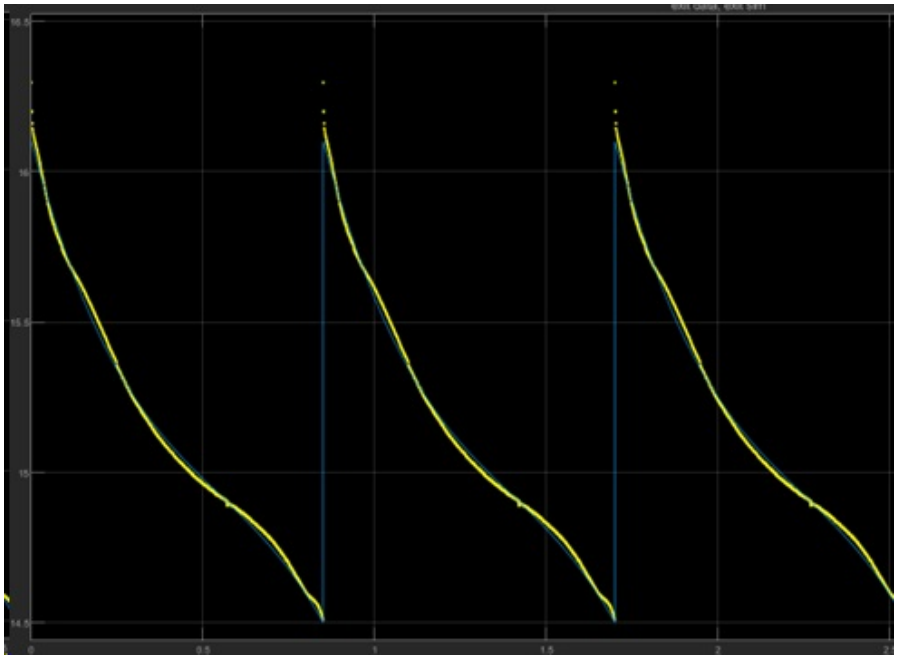

Figure 5.11: Simulation at 1C

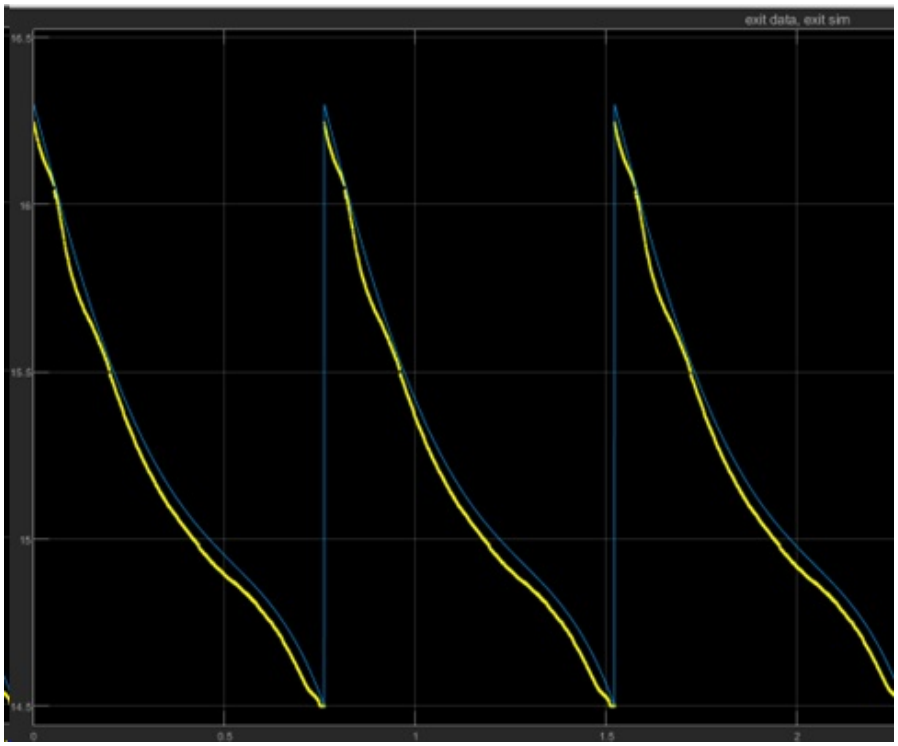

Figure 5.12: Simulation at 1.2C

As we can observe, the trends align quite well, which is a significant aspect of this analysis. The similarity in discharge time between the two curves is a crucial factor, and it's gratifying to see that this condition is met. It confirms that the simulation model is accurately replicating the real-world behavior of the battery, making it a reliable tool for further analyses and predictions.

However, it's also essential to acknowledge the slight discrepancies between the simulated and experimental curves. These differences can be attributed to several factors:

- Every experimental setup is subject to a degree of error.
- Instrument precision, calibration, and environmental factors can all introduce variations in the recorded data.
- The discharge current is not perfectly constant. Variations in load, internal resistance, and other factors can lead to fluctuations in the current, affecting the discharge curve.
- Unpredictable and random elements, including temperature variations, cell inconsistencies.

5.2 Simulink model

Now, we are moving forward to enhance the discharge model to incorporate a degradation model that accounts for the battery's capacity reduction over numerous cycles. A cycle is characterized by a complete charge and discharge phase of the battery. The objective is to develop a comprehensive model that not only simulates the charge and discharge processes but also counts the number of cycles completed. This count of cycles will serve as a crucial input for the capacity degradation model. The approach involves the use of a stateflow chart to seamlessly alternate between the charging and discharging phases while keeping an accurate count of the cycles. This integration aims to provide a holistic view of the battery's performance, endurance, and the inevitable decline in capacity, essential for predictive maintenance and operational efficiency.
In figure 5.13, we observe a model that simulates and counts the battery cycles. It incorporates two embedded subsystems that are activated only when specific conditions are met. This design enables the simulation of the alternating charging and discharging phases of the battery. Additionally, there is a stateflow chart in place that oversees the operations of the two subsystems and keeps a tally of the number of completed cycles.
To enhance the user interface and data visualization, a switch is incorporated. This switch ensures that the data displayed on the scope is from the appropriate subsystem, offering clarity and real-time insights into the ongoing phase, whether it is charging or discharging.

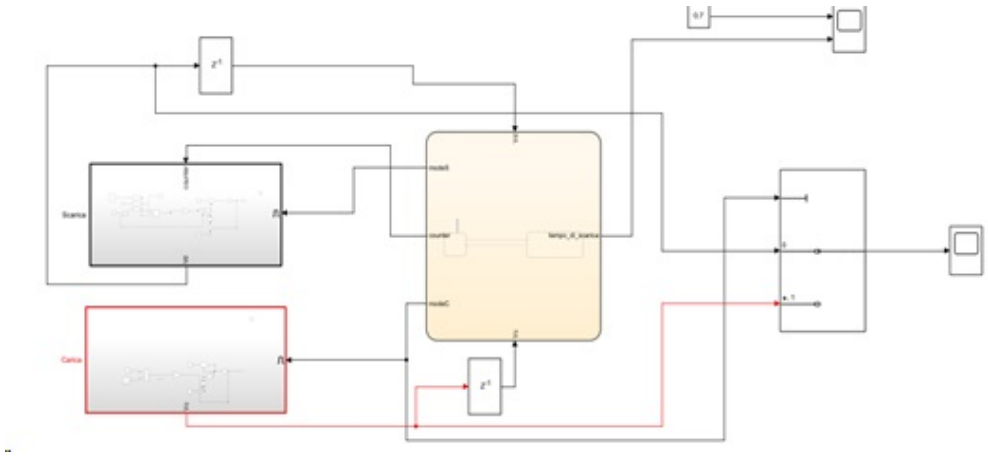

Figure 5.13: Cycle Simulation Model

The charge subsystem is designed to alternate the phases with the discharging process with certain simplifications to streamline the modeling process.
The charging current is set at a value of 5, reflecting a typical charging scenario. However, one of the key assumptions we've made is regarding the internal resistance of the battery. We've chosen to represent it as a constant, low-value resistance. This resistance encapsulates various factors that influence the battery's discharge process. The rationale behind this simplification is to capture the dominant behavior without getting entangled in the intricacies of minor variations.
The product of the charging current and this internal resistance gives us the voltage drop across the internal resistance. However, since we are in the charging phase, this voltage drop is added to the base voltage of 14.5V. This approach ensures that the model captures the increase in voltage as the battery charges. Additionally, there's a feedback loop integrated into the subsystem. This loop ensures that once the discharge phase concludes, the system resets, initiating a new charging cycle. This cyclical behavior is crucial for simulating repetitive charge-discharge cycles.
However, it's essential to note that the linear behavior described by this subsystem is a simplification. Given that we've used a constant value for the internal resistance, the model describes a linear charging trajectory. While this might not perfectly mirror the real-world behavior of the charging phase, it's a pragmatic choice. Typically, batteries are charged at low, constant currents over time. This means that variations in the charging behavior, especially those caused by fluctuating currents, have a minimal impact on the overall charge-discharge cycle.

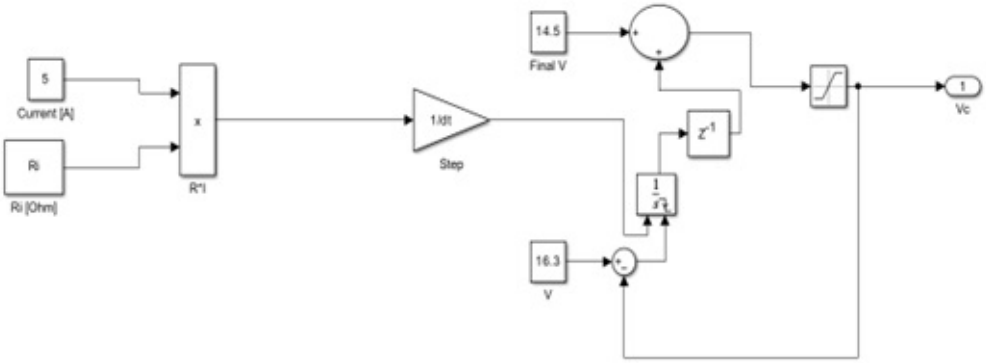

Figure 5.14: Charge subsystem

In the discharge subsystem, we commence with a constant block and an integrator to simulate time. This approach is crucial for defining the voltage trend over time during the discharge phase. To achieve this, we utilize a function block where a 4th-degree polynomial is applied. In the model depicted in Figure 51, we can observe two additional function blocks. These blocks receive the number of cycles and the c-rate as inputs. Through a defined relationship, they increment the voltage value, which subsequently needs to be accumulated every step and subtracted from the initial value of 16.3V. Additionally, another loop facilitates the resetting of the cycle, allowing the process to commence anew.

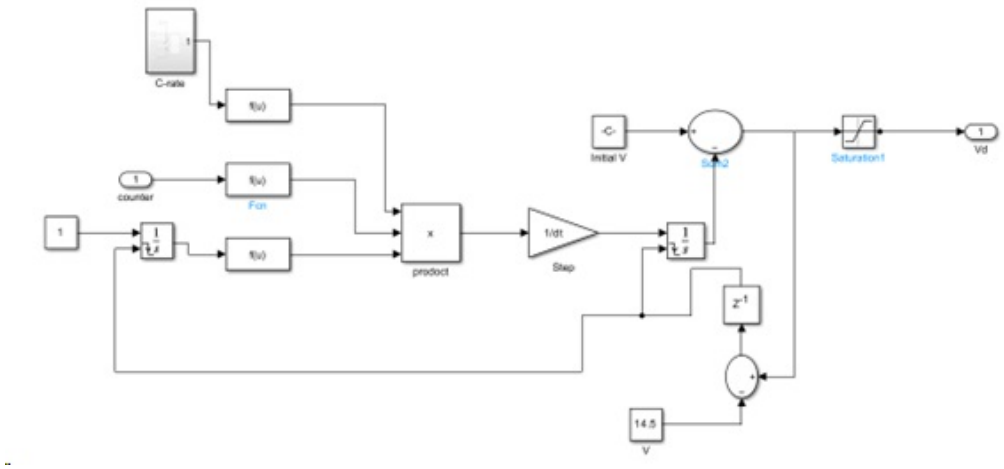

Figure 5.15: Discharge subsystem

Within the Stateflow framework, we initiate with a variable named 'counter', set at its genesis to zero. This variable serves to track the number of charge and discharge cycles the battery undergoes. Transitioning into the 'charging' state, we introduce an entry variable, 'modeC', set to 1. This move ensures that the charging subsystem is activated and remains operational until a specific condition is met: the battery voltage reaching the threshold of 16.3V. Upon achieving this voltage, a transition is triggered, and we exit the charging state. Concurrently, 'modeC' is reset to 0, effectively deactivating the charging subsystem and ensuring no further simulation occurs within this state.
Following this, the system seamlessly transitions into the 'discharge' state. Here, we set the 'modeS' variable to 1, activating the discharge subsystem. As the battery discharges, we employ the 'tc' variable to gauge the discharge duration. This temporal measurement is invaluable in understanding battery behavior under load. Furthermore, with each discharge cycle, the 'counter' variable is incremented, providing a cumulative tally of the cycles. Once the battery voltage dwindles to

14.5V, the system undergoes a state transition, reverting to the charging state. This cyclical process, oscillating between charging and discharging, continues, offering a dynamic and comprehensive simulation of the battery's operational lifecycle.

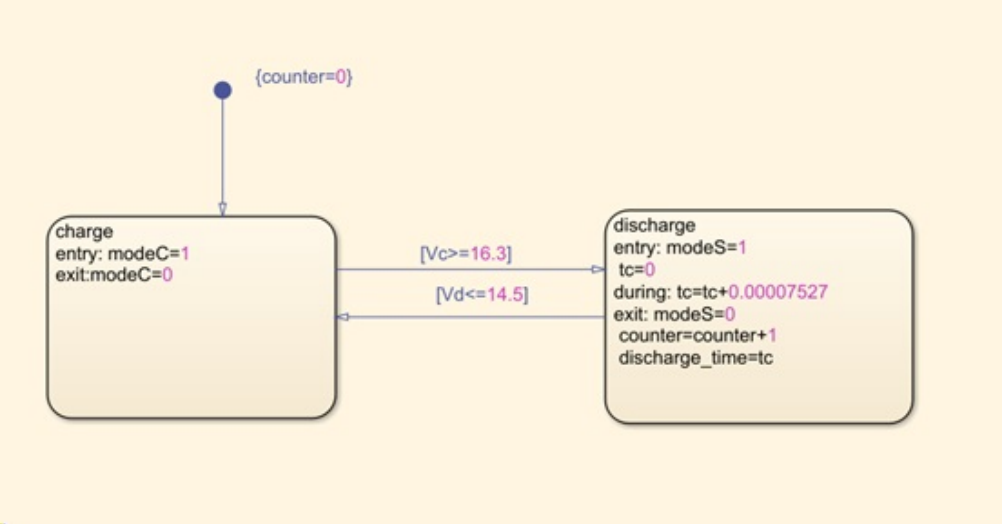

Figure 5.16: Stateflow Chart

As depicted in figure 5.16, the variables from the Stateflow chart, "modes" and "modec," activate the subsystems Discharge and Charge based on the current state. We can also observe the "counter" variable serving as an input to the "scarica" subsystem. This variable functions as a parameter for the capacity degradation model we have employed. Consequently, with each discharge cycle, there is a diminished capacity. Lastly, it is worth noting the presence of delay blocks, introduced to prevent algebraic loops.

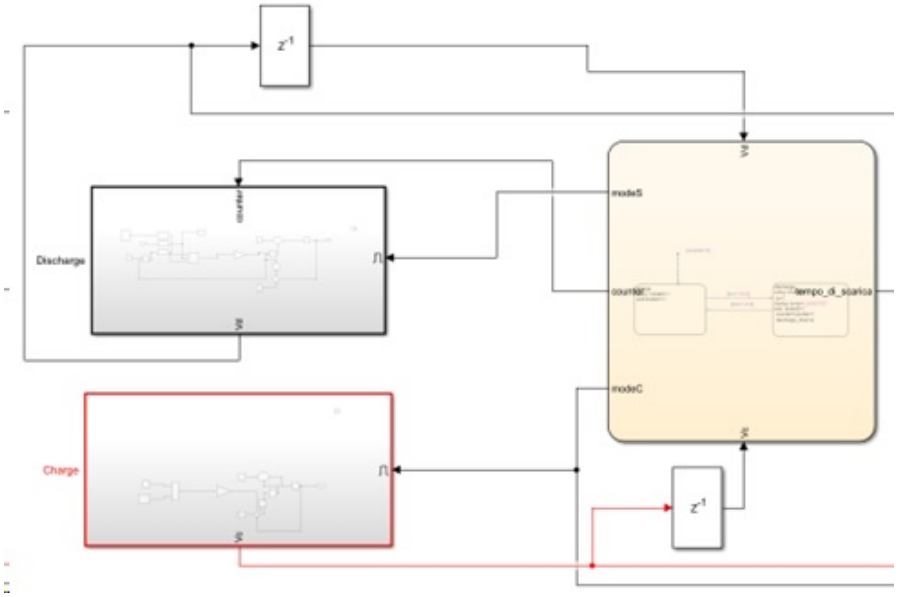

Figure 5.17: Connection between stateflow and subsystems

To accurately display the simulation, we utilize a switch block and the scope tool. The switch block is essential because we aim to visualize the voltage trend of the subsystem currently undergoing simulation. Thus, ports 0 and 1 represent the voltage outputs from the two subsystems. The control port is determined by the "modeC" variable. It's important to recall that the "modeC" variable holds a value of 1 when the "Charge" state is active and a value of 0 when the "discharge" state is inactive.

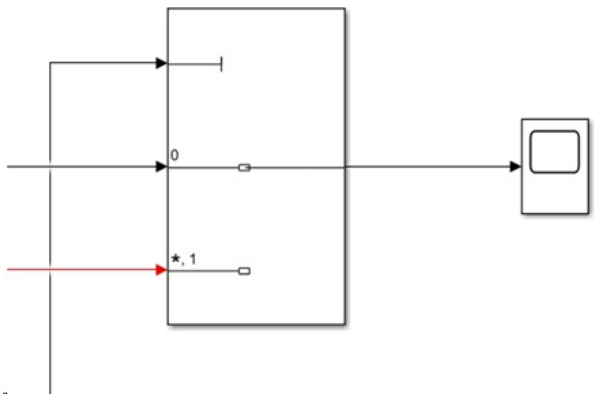

Figure 5.18: Switch block

5.3 Assumptions

In the current predictive model certain assumptions are indispensable. These assumptions not only simplify the intricate dynamics but also set the boundaries for the model's applicability. One of the most significant considerations in our model revolves around temperature dynamics. We chose to operate under a temperature-neutral environment. This decision, while seemingly simplistic, was rooted in pragmatism. Real-world battery cycles might indeed experience variable temperatures, but introducing this dynamic would have complicated the model especially in terms of data collection.
Voltage boundaries are another crucial aspect. Our model operates within a defined voltage range, starting at 16.3V and concluding at 14.5V. This decision was driven by safety considerations. LiPo batteries, can operate at voltages as low as 14.2V. However, given the known risks associated with LiPo batteries, we prioritized safety. This conservative approach, while ensuring safety, might introduce slight deviations when the model is applied in real-world scenarios where batteries are often pushed to their limits.
The model's approach to internal resistance during the charging phase is another point of discussion. We've assumed a consistent internal resistance, a decision rooted in the observation that at low charging currents, the impact of internal resistance on overall battery performance is minimal.
However, this might not lead to problems in the model since usually the charging current are low and constant. Another decision was to represent discharge curves using 4th-degree polynomial fits. Such polynomial fits offer a good accuracy. They are particularly effective in capturing the intricate trends we observed during our data collection phase.
Lastly, the model's paradigm around capacity degradation is noteworthy. We've leveraged a database centered on lithium-ion batteries, even when dealing with LiPo batteries. This decision was informed by the operational similarities between the two battery types. However, specific nuances unique to LiPo batteries might be overlooked, hinting at the potential benefits of a dedicated LiPo battery database.

5.4 Results

Let's dive into the findings. As mentioned earlier, one of our main goals was to determine the number of cycles the older battery underwent. To achieve this, we turned to a well-known capacity degradation model found in scientific literature, characterized by an exponential decay pattern: $f(t) = ae^{bt} + ce^{dt}$.

This model further provides a C-rate dependent relationship for the degradation of SOH over time, where one of its coefficients is described by: $d = ae^{\beta \times (\text{C-rate})^2}$.

As we can see in figure 5.19, the plotted curves represent the percentage of capacity loss across various C-rates, ranging from 0.5 to 1.2. The difference in discharge current isn't too vast, it's notable that the curves are closely aligned with one another indicating that, within the studied range, the battery's degradation behavior exhibits minimal variance with changes in C-rate.

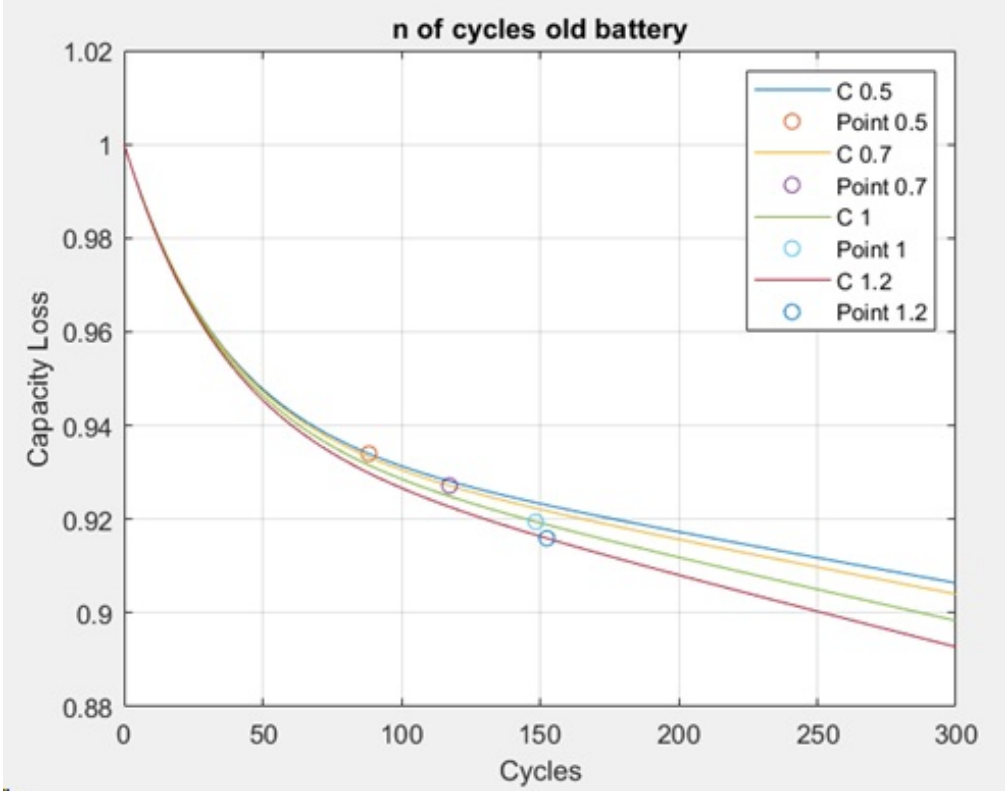

Figure 5.19: Capacity loss

By integrating the capacity differences observed between the old and new batteries from our experimental tests, we can pinpoint four distinct markers corresponding to the four C-rates. A closer examination, as depicted in figure 5.20, shows where these markers intersect with the degradation curves. These intersections help us determine the estimated number of cycles the older battery has undergone. It's crucial to note that we don't arrive at a single, precise number but rather a range of possible values.
A specific observation needs to be made concerning the 0.5C curve. This current value doesn't mirror the battery's real-world use. The minimum current typically used for these batteries aligns with the charging current, which is at 0.7C. As a result, any findings associated with the 0.5C curve may not be trustworthy and can be disregarded for practical purposes.

In contrast, the curves for C-rates 1 and 1.2 are more reflective of how the battery is typically used in real-life scenarios, making their results more credible. As we observe, the range for the number of cycles the older battery might have undergone falls between 115 to 155 cycles.

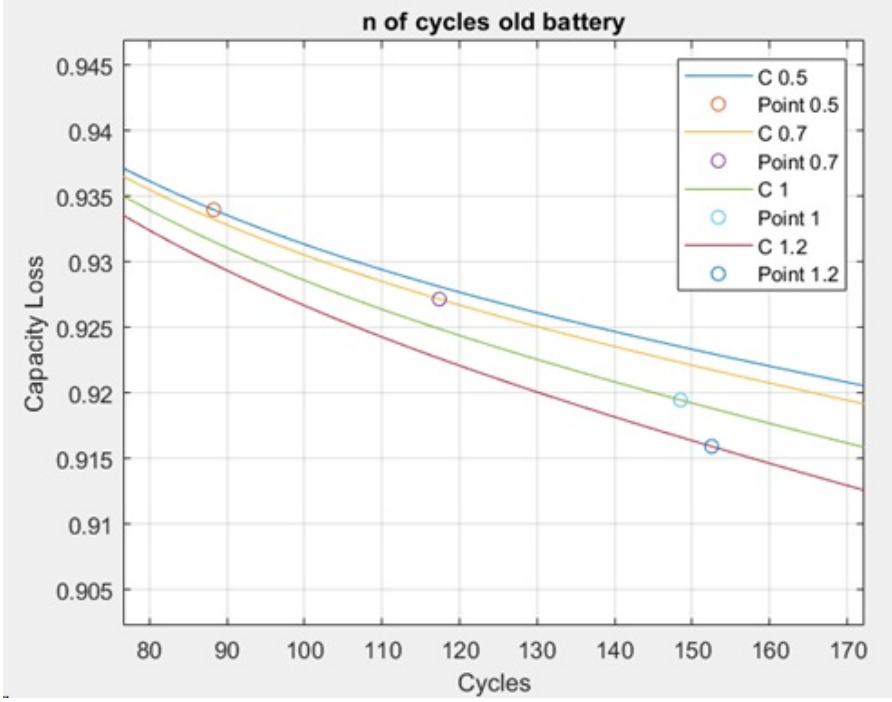

Figure 5.20: Range of possible cycles

By incorporating these degradation models into the functions of the Simulink model, specifically within the "discharge" subsystem, we're able to simulate the battery's charge and discharge cycles. Figure 5.21 provides a snapshot of such a simulation, where we can distinctly identify both the charging and discharging phases across multiple cycles.
The simulation's primary objective is to start from the performance metrics of a new battery. As we simulate subsequent charge and discharge cycles, the model introduces a gradual reduction in battery capacity based on the number of cycles completed. This continues until the simulated battery's performance aligns with that of the old battery.
After reaching this point, the simulation can further proceed to forecast the battery's degradation until it hits a performance level deemed as the threshold or limit. This specific point on the degradation model is referred to as the "knee", a juncture where the battery's capacity degradation accelerates. Drawing from existing literature, this threshold typically corresponds to an 80% capacity loss.

Once this threshold is reached, we can extrapolate how many more life cycles the older battery has before it's deemed non-functional or significantly inefficient for practical applications.

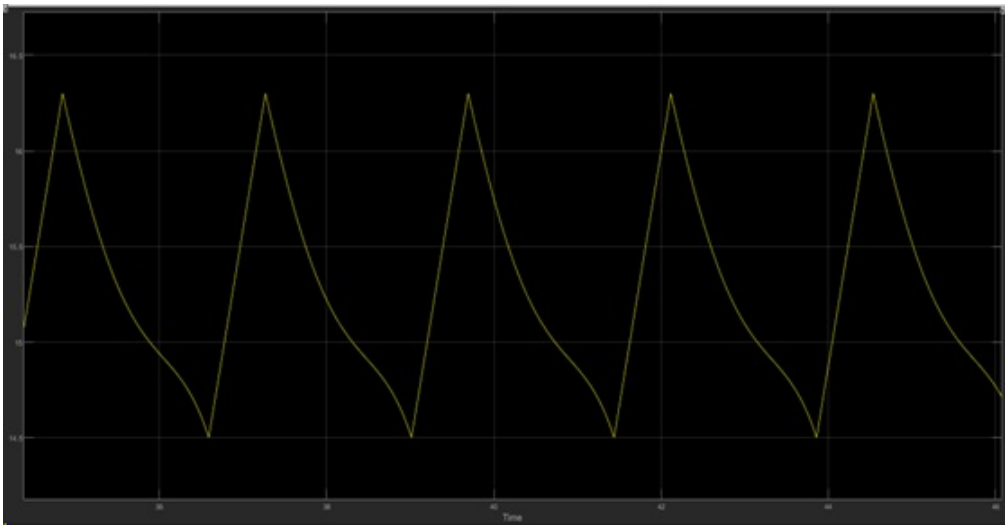

Figure 5.21: Cycles simulation

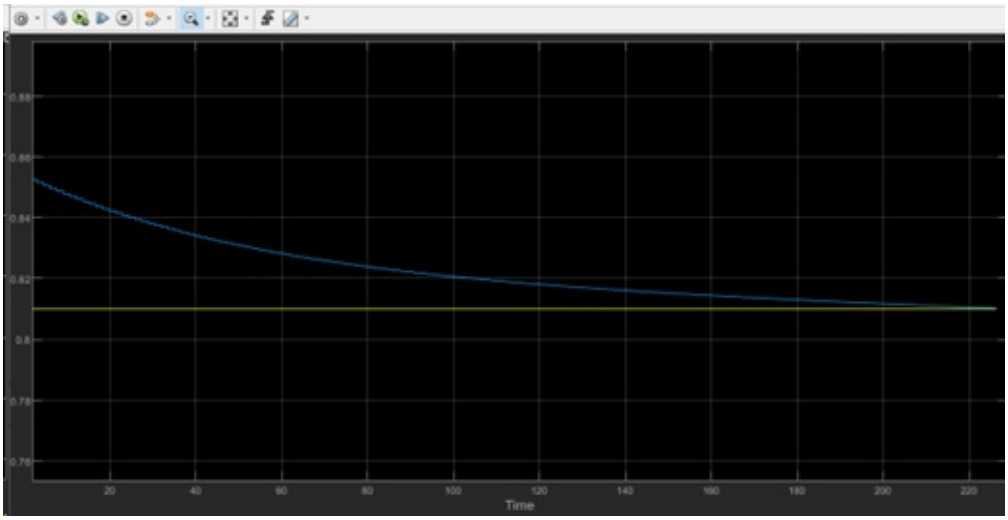

Figure 5.22: Model simulation

In figure 5.22, we get a visual representation of the simulation. The yellow line on the graph signifies the target value, representing the capacity of the old battery. The blue line, on the other hand, showcases the capacity of the new battery. As the graph reveals, this capacity undergoes degradation over time. The x-axis marks

the simulation time. From the simulation, the result shows that the new battery requires 149 cycles at a C-rate of 1 to degrade to the performance level of the old battery. From this, we can deduce that the "old" battery still retains a significant amount of its original capacity and can thus be used for numerous additional cycles before reaching the end of its functional lifespan.

Chapter 6

Conclusions and future developments

6.1 Conclusions

In this study, we designed a test bench specifically to record the voltage and current data of a battery throughout its charging and discharging cycles. A pivotal consideration was maintaining consistency in experimental conditions when examining both new and old batteries. This especially included temperature control, ensuring its influence was eliminated, providing a neutral testing environment. The experimentation started with the new battery. We subjected the battery to various C-rates: 0.5C, 0.7C, 1C, and 1.2C. The data curves revealed a pronounced decline in voltage as time progressed. This voltage dynamic was noticeably impacted by the discharge current. Specifically, an increase in discharge current corresponded with a faster voltage drop, reaching a low of 14.5 V in a considerably shorter period. From our observations, a tangible difference emerged in the discharge times when the battery was exposed to different discharge currents. Comparing these durations revealed a marked reduction in the autonomy of the aged battery when placed alongside its newer counterpart, pointing towards battery degradation. This revelation, while not immediately intuitive, is paramount as it provides deep insights into battery behavior.
Turning to academic sources, we incorporated a capacity degradation model. This model consistently showcased an exponential decay pattern. Additionally, we integrated a C-rate dependent model into our framework. By synthesizing the data from the degradation model and our experimental findings on capacity loss, we inferred that the aged battery had experienced between 115 to 155 cycles. this range offers a probabilistic understanding of the issue. This approach acknowledges the inherent uncertainties and variations in real-world scenarios. The range offers

a degree of confidence about where the true value likely lies.

6.2 Potential future developments

One of the most palpable constraints faced was the reliance on experimental data from just two batteries. Such a limited dataset can lack on reliability, or at the very least, not capture the full spectrum of potential battery behaviors. An avenue worth exploring would be the acquisition of a more extensive database that pools data from a multitude of LiPo batteries. Such a repository would undoubtedly enhance the accuracy of the study, rendering the conclusions more robust and reliable. This broader dataset would not only help refine the results but also facilitate a more in-depth analysis of the inherent uncertainties of the results. By delving into the variability and scatter of the collected data, one could assess the confidence levels of the conclusions reached and identify potential anomalies.
Another study worth doing is evaluating the impact of temperature on battery performance. Temperature, known to exert significant influence over the internal chemical reactions of batteries, can modulate the discharge and charge cycles noticeably. By weaving in the temperature variable, future research iterations can offer a model that's more attuned to real-world scenarios. Moreover, while the current investigation was circumscribed to specific C-rates, expanding the horizon to include higher C-rates might reveal battery behavior nuances under more aggressive or demanding operational conditions. Such an exploration can be invaluable, especially for applications that require rapid discharges or are subjected to high-power demands.

Bibliography

[1] Dian Wang, Yun Bao, and Jianjun Shi. «Online Lithium-Ion Battery Internal Resistance Measurement Application in State-of-Charge Estimation Using the Extended Kalman Filter». In: *Energies* (2017).

[2] Peter M Attia et al. «Review—"Knees" in Lithium-Ion Battery Aging Trajectories». In: *Journal of The Electrochemical Society* (2022).

[3] Simon E. J. O'Kane et al. «Lithium-ion battery degradation: how to model it». In: *PCCP* (2022).

[4] Jacqueline S. Edge et al. «Lithium ion battery degradation: what you need to know». In: *PCCP* (2022).

[5] Aramis Perez, Vanessa Quintero, Francisco Jaramillo, Heraldo Rozas, Diego Jimenez, Marcos Orchard, and Rodrigo Moreno. «Characterization of the Degradation Process of Lithium-ion Batteries when Discharged at Different Current Rates». In: *Sagepub* (2016).

[6] Marcus Johnen, Simon Pitzen, Udo Kamps, Maria Kateri, and Dirk Uwe Sauer. «Modeling Long-Term Capacity Degradation of Lithium-Ion Batteries». In: *stat.AP* (2019).

[7] Y. Wang, S. Tseng, B. Lindqvist, and K. Tsui. «End of Performance Prediction of Lithium-Ion Batteries». In: *Journal of Quality Technology* (2019).

[8] Y. Xing, E. W. Ma, K.-L. Tsui, and M. Pecht. «An Ensemble Model for Predicting the Remaining Useful Performance of Lithium-Ion Batteries». In: *Microelectronics Reliability* (2013).

[9] H. J. Bergveld, W. S. Kruijt, and P. H. L. Notten. «Battery State-of-Charge Indication». In: (2002).

[10] George E. Gorospe Jr and Chetan S. Kulkarni. «A Novel UAV Electric Propulsion Testbed for Diagnostics and Prognostics». In: ().

[11] D. Belov and M.-H. Yang. «Failure Mechanism of Li-ion Battery at Overcharge Conditions». In: *Journal of Solid State Electrochemistry* (2008).

[12] Abhinav Saxena, Brian Bole, Matthew Daigle, and Kai Goebel. «Prognostics for Batteries Aging Experiments and Modeling». In: (2012). Presented at NASA Battery Workshop 2012.

[13] Renato G. Nascimento, Felipe A. C. Viana, Matteo Corbetta, and Chetan S. Kulkarni. «A framework for Li-ion battery prognosis based on hybrid Bayesian physics-informed neural networks». In: *Scientific Reports* (2022). URL: www.nature.com/scientificreports.

[14] L. Zheng, L. Zhang, J. Zhu, G. Wang, and J. Jiang. «Co-estimation of state-of-charge, capacity and resistance for lithium-ion batteries based on a high-fidelity electrochemical model». In: *Applied Energy* (2016). URL: https://doi.org/10.1016/j.apenergy.2016.08.016.

[15] Francesco Cadini, Claudio Sbarufatti, Francesco Cancelliere, and Marco Giglio. «A Data-Driven Particle Filter for Lithium-Ion Batteries State-of-Life Prognosis». In: (2018).

[16] M. B. Pinson and M. Z. Bazant. «Theory of SEI Formation in Rechargeable Batteries: Capacity Fade, Accelerated Aging and Lifetime Prediction». In: *Journal of the Electrochemical Society* (2012). URL: https://doi.org/10.1149/2.044302jes.

[17] B. Saha and K. Goebel. «Battery Data Set». In: (2007). URL: https://ti.arc.nasa.gov/tech/dash/pcoe/prognostic-data-repository/#battery.

[18] J. Vetter, P. Novák, M. R. Wagner, C. Veit, K. C. Möller, J. O. Besenhard, et al. «Ageing mechanisms in lithium-ion batteries». In: *Journal of Power Sources* (2005).

[19] D. Wang, F. Yang, Y. Zhao, and K.-L. Tsui. «Battery remaining useful life prediction at different discharge rates». In: *Microelectronics Reliability* (2017).

[20] Soyoung Lee, Jaehyeok Doh, and Jongsoo Lee. «Prognosis of Lithium-ion Batteries: Considering Cycle and Storage Conditions». In: Prognostics and Health Management Society. 2018.

[21] Tyto Robotics. *Tyto Robotics*. 2023. URL: https://www.tytorobotics.com/.

[22] Battery University. *Battery University*. 2023. URL: https://batteryuniversity.com/.

[23] M. Daigle and C.S. Kulkarni. «Electrochemistry-based Battery Modeling for Prognostics». In: *Annual Conference of the Prognostics and Health Management Society 2013*. PHM Society. 2013.

[24] M. Berecibar, I. Gandiaga, I. Villarreal, et al. «Critical review of state of health estimation methods of li-ion batteries for real applications». In: *Renewable and Sustainable Energy Reviews* (2016).

[25] D. Andre, C. Appel, T. Soczka-Guth, et al. «Advanced mathematical methods of SOC and SOH estimation for lithium-ion batteries». In: *Journal of Power Sources* (2013).

[26] G. Ning, B. Haran, and B. N. Popov. «Capacity Fade Study of Lithium-Ion Batteries Cycled at High Discharge Rates». In: *Journal of Power Sources* (2003).

[27] G. Ning, R. E. White, and B. N. Popov. «A Generalized Cycle Life Model of Rechargeable Li-ion Batteries». In: *Electrochimica Acta* (2006).

[28] G. Ning and B. N. Popov. «Cycle Life Modeling of Lithium-Ion Batteries». In: *Journal of The Electrochemical Society* (2004).

[29] J. Zhang and J. Lee. «A Review on Prognostics and Health Monitoring of Li-ion Battery». In: *Journal of Power Sources* (2011).